

Kinematics and Dynamics of the Galactic Bar revealed by *Gaia* Long Period Variables

Han-Yuan Zhang,^{1*} Vasily Belokurov¹, N. Wyn Evans¹, Sarah G. Kane¹ and Jason L. Sanders²

¹ *Institute of Astronomy, University of Cambridge, Madingley Road, Cambridge CB3 0HA, UK*

² *Department of Physics and Astronomy, University College London, London WC1E 6BT, UK*

Accepted XXX. Received YYY; in original form ZZZ

ABSTRACT

We take low-amplitude, long period variable (LA-LPV) candidates in *Gaia* DR3 as tracers of the kinematics and dynamics of the Milky Way bar. LA-LPVs, like other LPVs, have high luminosities and follow a tight period-luminosity relation, but unlike e.g. Mira variables, their radial velocity measurements are reliable due to their smaller pulsation amplitudes. We supplement the *Gaia* astrometric and radial velocity measurements with distance moduli assigned using a period-luminosity relation to acquire full 6D phase space information. The assigned distances are validated by comparing to geometric distances and StarHorse distances, which shows biases less than $\sim 5\%$. Our sample provides an unprecedented panoramic picture of the inner Galaxy with minimal selection function effects. We map the kinematics of the inner Milky Way and find a significant kinematic signature corresponding to the Galactic bar. We measure the pattern speed of the Galactic bar using the continuity equation and find $\Omega_b = 34.1 \pm 2.4 \text{ km s}^{-1} \text{ kpc}^{-1}$. We develop a simple, robust and model-independent method to measure the dynamical length of the bar using only kinematics and find $R_b \sim 4.0 \text{ kpc}$. We validate both measurements using N-body simulations. Assuming knowledge of the gravitational potential of the inner Milky Way, we analyse the orbital structure of the Galactic bar using orbital frequency ratios. The x_1 orbits are the dominant bar-supporting orbital family in our sample. Amongst the selected bar stars, the $x_1 v_1$ or "banana" orbits constitute a larger fraction ($\sim 15\%$) than other orbital families in the bar, implying that they are the dominant family contributing to the Galactic X-shape, although contributions from other orbital families are present.

Key words: Galaxy: bulge – Galaxy: centre – Galaxy: kinematics and dynamics – stars: variables: general – Galaxy: structure

1 INTRODUCTION

There is no doubt today that the Milky Way hosts an elongated, non-axisymmetric bar at the centre, a common feature for disc galaxies. The Milky Way bar was first observed in non-axisymmetric gas flow (Peters 1975; Binney et al. 1991), near-infrared emission (Blitz & Spergel 1991) and star counts (Nakada et al. 1991; Stanek et al. 1997). A revolution in the understanding of the Galactic bar has occurred in the past two decades using red clump stars as standard candles due to their narrow luminosity function (McWilliam & Zoccali 2010; Nataf et al. 2010). Without resolving the locations of individual stars, the distribution of red clump stars can be inferred statistically by inverting the observed luminosity function along each line-of-sight (see Wegg & Gerhard 2013). 3D density maps

of the inner Galaxy are constructed using this technique (Wegg & Gerhard 2013; Wegg et al. 2015; Simion et al. 2017; Sanders et al. 2019a; Paterson et al. 2020). Augmenting the 3D density distribution of the inner Galaxy with kinematics from the BRAVA and ARGOS surveys, Portail et al. (2015a, 2017) built dynamical models and found the effective potential of the Galactic bar using the made-to-measure (M2M) method. Orbital structures of the Galactic bar in the M2M models were analysed in Portail et al. (2015b).

The pattern speed of the Galactic bar is a crucial parameter because it sets the resonance radii for stars and affects the kinematics in the solar neighbourhood (Binney 2020; Kawata et al. 2021), in the disc (Chiba & Schönrich 2021; Gaia Collaboration et al. 2023b) and in the halo (Davies et al. 2023; Dillamore et al. 2023, 2024). Older measurements of gas kinematics reported a fast-short bar with a pattern speed of $50 - 60 \text{ km s}^{-1} \text{ kpc}^{-1}$ (Fux 1999; Englmaier & Gerhard 1999), while more recent measurements of gas give a

* hz420@cam.ac.uk (HZ)

smaller value of $40 \text{ km s}^{-1} \text{ kpc}^{-1}$ (e.g. [Sormani et al. 2015](#); [Li et al. 2022](#)). Compared to the relatively fast pattern speed measured from gas kinematics, observations of the resonance features in the solar neighbourhood give a slower pattern speed in the range of $34 - 40 \text{ km s}^{-1} \text{ kpc}^{-1}$ ([Binney 2020](#); [Chiba & Schönrich 2021](#); [Kawata et al. 2021](#); [Gaia Collaboration et al. 2023b](#); [Dillamore et al. 2023, 2024](#)). Directly observing the central region of the Galaxy, [Clarke & Gerhard \(2022\)](#) measured a pattern speed of $\sim 33 \text{ km s}^{-1} \text{ kpc}^{-1}$ using M2M method with *Gaia* and VIRAC proper motion measurements. Applying the continuity equations to the stars at the inner Milky Way yielded a pattern speed of $\sim 41 \text{ km s}^{-1} \text{ kpc}^{-1}$ ([Sanders et al. 2019b](#); [Bovy et al. 2019](#); [Leung et al. 2023](#)).

Parallax measurements from *Gaia* are usually imprecise in the region of the Galactic bar ([Bailer-Jones et al. 2021](#)). Previous attempts to acquire full 6D phase space measurements rely on the spectroscopy-based distances (StarHorse and AstroNN, [Bovy et al. 2019](#); [Queiroz et al. 2020, 2021](#); [Ardern-Arentsen et al. 2024](#)), which therefore have strong selection functions. The heavy dust extinction also induces an additional selection function at the inner Galaxy, further complicating studies of the Galactic bar. In this work, we use the period-luminosity relations (PLR) of long period variables (LPV) to assign the distances instead. Structures in the Milky Way have been intensively studied using variables as tracers because of their tight PLR, most famously RR Lyrae ([Prudil et al. 2022](#); [Semczuk et al. 2022](#)) and Cepheid variables ([Lemasle et al. 2022](#); [Matsunaga et al. 2023](#)). However, both are biased tracers – RR Lyrae are typically old, while (classical) Cepheids are younger. LPVs, as another type of pulsating star, exhibit longer period pulsations ranging from 10 days to greater than 1000. LPVs follow tight PLRs and can be used as distance indicators ([Rau et al. 2019](#); [Trabucchi et al. 2021](#); [Sanders 2023](#)). Also, because LPVs are redder than RR Lyrae and Cepheids, they are less affected by dust extinction. Hence, LPVs are popularly used to trace the structure of the Milky Way ([Catchpole et al. 2016](#); [Grady et al. 2020](#); [Sanders et al. 2022](#); [Iwanek et al. 2023](#); [Hey et al. 2023](#); [Sanders et al. 2024](#)). Among several types of LPVs, Mira variables have a unique property wherein the period and age are correlated ([Feast & Whitelock 2000](#); [Grady et al. 2019](#); [Trabucchi & Mowlavi 2022](#); [Zhang & Sanders 2023](#)). The ages of Mira variables range from ~ 2 to 12 Gyr, implying that these LPV tracers are an unbiased tracer of the underlying wide mix of stellar populations. The period-age relation in [Zhang & Sanders \(2023\)](#) can be used to date the formation epoch of the Galactic bar ([Sanders et al. 2024](#)).

In this paper, we use OSARGs (OGLE Small Amplitude Red Giants, [Wray et al. 2004](#)) instead of Mira variables as tracers. Due to the low amplitude of OSARGs' pulsation, in this paper, we also refer to them as low-amplitude, long-period variables (LA-LPV). LA-LPVs have characteristic periods between 0 to over 100 days and are more abundant than Miras. They serve as distance indicators with uncertainties smaller than $\sim 15\%$ ([Rau et al. 2019](#); [Hey et al. 2023](#)). Light curves of LA-LPVs show multi-periodic behaviour and small amplitude fluctuations with G amplitude $\lesssim 0.2$ ([Soszyński et al. 2004](#)). They are distinguished from other LPVs by their distinct PLRs ([Wood 2000](#); [Soszyński et al. 2007](#)), which have smaller periods and fainter brightness compared to Miras and semi-regular variables (SRV). LA-LPVs are better kinematics tracers than Mira variables because their pulsation amplitudes are smaller, so radial velocity measurements from *Gaia* remain useful. The OGLE survey ([Udalski et al. 1992](#)) discovered and investigated OSARGs in detail with selected candidates in the LMC, SMC ([Soszyński et al. 2009](#)) and the Galactic bulge ([Soszyński et al. 2013](#)). [Hey et al. \(2023\)](#) used LA-LPV and SRV candidates in the OGLE-BLG

survey ([Soszyński et al. 2013](#)) to investigate the kinematics of the Galactic bar. They found a clear quadrupole pattern in the velocity field corresponding to the bar, but the presence of a selection function caused by the OGLE footprint made further quantitative analysis difficult. In this work, we explore the *Gaia* LPV catalogue ([Eyer et al. 2023](#); [Lebzelter et al. 2023](#)). Thanks to the full-sky coverage of *Gaia*, there is no sharp truncation at the edge of the OGLE footprint in our LA-LPV sample compared to the sample in OGLE-BLG ([Hey et al. 2023](#)). Therefore, we can build a panoramic view of the inner Galaxy with resolved stars using the full 6D phase space, which allows us to study the kinematics and dynamics of the Galactic bar in detail.

This paper is structured as follows: we present the catalogue construction and distance assignment in section 2. In section 3, we map the kinematics of the Galactic centre and compare our observational results with simulations. We also quantify the pattern speed and bar length solely using stellar kinematics. We investigate the dynamical properties and orbital structures of the LPV tracers in section 4. In section 5, we discuss and compare our pattern speed and bar length measurements with previous studies. We conclude our analysis in section 6.

2 DATA

2.1 Gaia Long Period Variables

We use the specific object study (SOS) table from the LPV catalogue of *Gaia* DR3 ([Lebzelter et al. 2023](#); [Gaia Collaboration et al. 2023a](#)) to select LA-LPV candidates. This catalogue is constructed using supervised classification of identified variable stars in *Gaia* data with features including parallax, colours, light curve statistics and Lomb-Scargle period ([Eyer et al. 2023](#)). Stars classified as LPVs that have the 5th-95th percentile of their G-band light curves greater than 0.1 mag and $G_{BP} - G_{RP} > 0.5$ (together with some other minor cleaning cuts) enter the final SOS table (see details in [Lebzelter et al. 2023](#)). [Eyer et al. \(2023\)](#) compared the SOS LPV catalogue with the ASAS-SN ([Kochanek et al. 2017](#)) survey and the OGLE ([Udalski et al. 1992](#)) survey and found a contamination of $\sim 1\%$.

The periods of the identified LPVs in the SOS table are determined from the G light curves using the generalised Lomb-Scargle periodogram ([VanderPlas 2018](#)). Periods are only published if the primary period is greater than 35 days and smaller than 34 months (the duration of the time series). The amplitude corresponds to the half peak-to-peak amplitude of the fundamental Fourier mode. Due to the amplitude and period cut in the *Gaia* LPV catalogue, small amplitude LA-LPVs on the fainter magnitude end are excluded.

We acquire the infrared photometry of the *Gaia* LPV candidates from the 2MASS catalogue ([Skrutskie et al. 2006](#)) using a cross-match with $1''$ radius. Removing stars with low-quality JHK_s measurements by requiring `ph_qual=AAA` and `gal_contam = 0`, we retain 131,561 LPV candidates with valid J and K_s band photometry. We compute the colour-corrected Wesenheit index W_{JK_s} using

$$W_{JK_s} = K_s - 0.686 \times (J - K_s), \quad (1)$$

and we define the absolute magnitude corresponding to W_{JK_s} as M_{JK_s} ([Cardelli et al. 1989](#); [Soszyński et al. 2007](#)). Although the extinction law at the inner Galaxy is flatter than the one used in [Cardelli et al. \(1989\)](#), we treat this as a second-order effect ([Nishiyama et al. 2009](#)).

2.2 Selection of LA-LPV candidates in the *Gaia* LPV catalogue

We start by selecting stars sitting on the period-luminosity ridges of OSARGs (sequence A and B in Wood 2000) and Long Secondary Period (LSP, sequence D). The physical origin of these pulsation sequences is still under debate, but for our purposes all that matters is that they are empirically secure. OSARGs are characterised by their small amplitudes (typically G amplitude $\lesssim 0.2$ mag) and multi-periodic behaviour. The periods of OSARGs are mainly in the range of 10 to 100 days; however, many OSARGs also have characteristic periods longer than 200 days associated with the LSP. Rau et al. (2019) demonstrated the correlation between the period, luminosity and amplitude of OSARGs. Because the *Gaia* LPV catalogue only provides the primary period and corresponding amplitude, selecting OSARGs using their multi-periodic signatures from this catalogue is challenging. Hence, we turn to the period and amplitude features. In the top panel of Fig. 1, we plot LPV candidates in the OGLEIII-LMC survey (Soszyński et al. 2009) in the period-luminosity (M_{JKs}) plane. LPV candidates with I amplitudes of the pulsation mode between 0.02 and 0.06 are overlaid as aqua dots, and the 2D histogram of the number counts of all LPV candidates (amplitude range spans from 0.01 to ~ 0.2) is plotted in the background. The period- M_{JKs} relation becomes less complicated after cutting $0.02 < I$ amplitude < 0.06 , in which only three prominent sequences are left. The two main ridges corresponding to the main OSARG and LSP period- M_{JKs} relations are denoted by the red and blue dashed lines, which are the PLR calibrated in Soszyński et al. (2007). For now, we neglect the secondary OSARG sequence on the leftmost side of the plane as it is a subdominant population.

Inspecting the period- M_{JKs} sequences of LPVs in the Milky Way, we select stars with high-quality parallax using fractional parallax uncertainty, $\sigma_{\varpi}/\varpi < 0.05$, and we plot them on the period- M_{JKs} plane as shown in the lower panel of Fig. 1, where the distance moduli are computed using geometric distances from Bailer-Jones et al. (2021). We find multiple sequences in the window for the LSP period-luminosity sequence due to the presence of SRVs and Mira variables. However, different sequences can be well distinguished using the amplitude of the pulsation mode, as SRV and Mira variables have larger G amplitudes than OSARGs (Soszyński et al. 2007; Matsunaga et al. 2009; Grady et al. 2019). LPVs with G amplitude < 0.15 are shown by the black dots, and on those two unshaded regions, the period-luminosity sequences of OSARGs and LSPs are conspicuous and denoted by the red and blue solid lines. Therefore, we remove stars with G amplitude > 0.15 to isolate LA-LPV candidates from the *Gaia* LPV catalogue.

We further clean the LA-LPV candidates from young stellar object (YSO) contamination, as YSOs share similar colours, amplitudes and periods with LPVs (Mowlavi et al. 2018). Zhang & Sanders (2023) showed that the `best_class_score`, the probability of the object being the reported class from the classification pipeline, is useful to remove potential YSO contamination. Hence, we cut using `best_class_score` > 0.8 . We also remove stars with primary periods between $1.9 < \log_{10}(\text{Period}/\text{days}) < 2.4$ and $\log_{10}(\text{Period}/\text{days}) > 2.9$ to clean LA-LPV stars that are not sitting on OSARG or LSP period-luminosity tracks as shown by the grey shaded region in Fig. 1.

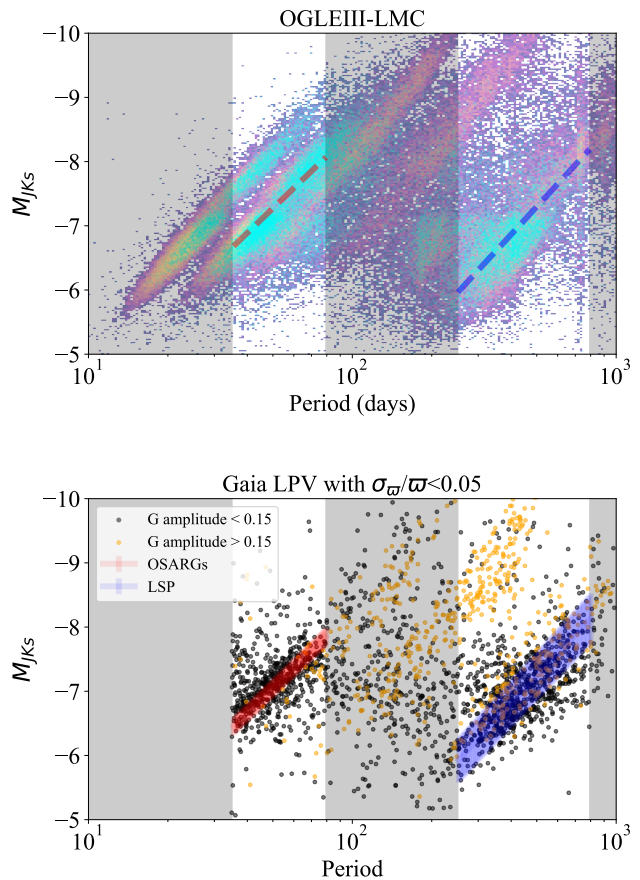


Figure 1. In the upper panel, we plot all LPV candidates in OGLEIII-LMC in $P - M_{JKs}$ plane at the background. Each of those stars has up to three reported periods and associated amplitudes, so a star can contribute three times to the 2D histogram. The foreground aqua dots are pulsation modes with I amplitude between 0.02 and 0.06 to illustrate the power of amplitude cuts on cleaning the $P - M_{JKs}$ sequences. In the lower panel, we plot the same plane for the *Gaia* LPV catalogue with $\sigma_{\varpi}/\varpi < 0.05$, and the distance modulus is computed using the geometric distance from Bailer-Jones et al. (2021). *Gaia* LPV candidates are coloured according to their reported amplitude, where stars with G amplitude smaller than 0.15 are black, and other stars are orange. The red and blue lines are the fitted OSARG and LSP period-luminosity sequence, and the width of the line represents the 1σ intrinsic scatter in the sequence. In both plots, we mask the period ranges that we exclude when constructing the final sample.

2.3 Distance Assignment using the Period-luminosity Relation

Due to the sparse sampling of the *Gaia* light curves, the period uncertainties are significantly larger than those from OGLE. The intrinsic scatter in the PLR, the period uncertainty, and the magnitude scatter from single-epoch 2MASS photometry all broaden the width of the period- M_{JKs} sequence in *Gaia* data. Hence, instead of calibrating the period- M_{JKs} relation of OSARGs and LSPs from the *Gaia* LPV catalogue, we use the parametrised period- M_{JKs} relation calibrated in Soszyński et al. (2007) and treat the uncertainty on the fitted parameters therein as the intrinsic scatter of the period-luminosity relation. Soszyński et al. (2007) fitted W_{JKs} as a linear function of $\log(P)$ in the form

$$W_{JKs} = \alpha \log(P) + \beta \quad (2)$$

where P is the period of the pulsation mode. We convert W_{JKs} to M_{JKs} using the LMC distance modulus of 18.48 (Pietrzyński et al. 2019). As shown in Tabur et al. (2010), the period-luminosity sequence of OSARGs shifts slightly when surveys use different amplitude cuts due to the correlation in the period-luminosity and amplitude. Therefore, to adapt the amplitude cut in the *Gaia* LPV catalogue (and also the Milky Way environment), we further introduce an offset and fit the offset using stars in *Gaia* LPV with $\varpi/\sigma_{\varpi} > 20$, i.e. re-calibrate the P - M_{JKs} relation using black dots in the lower panel of Fig. 1. The adapted parameters in Eq. 2 are $\alpha_{\text{OSARG}} = -3.96 \pm 0.04$ and $\beta_{\text{OSARG}} = -17.95 \pm 0.13$; $\alpha_{\text{LSP}} = -4.40 \pm 0.11$ and $\beta_{\text{LSP}} = -23.41 \pm 0.23$. Compared to the PLR in Soszyński et al. (2007), both OSARGs and LSP sequences have offsets on the order of ~ 0.2 mag. The discussion of the exact causes of this offset is beyond the scope of this work. These two sequences are shown as the red and blue thick lines in the lower panel of Fig. 1, where the width of the lines shows 1σ scatter of the P - M_{JKs} relation when the period uncertainty is 0. We assign M_{JKs} to stars with the *Gaia* period between $1.6 < \log(P/\text{day}) < 1.9$ using α_{OSARG} and β_{OSARG} and stars with $2.4 < \log(P/\text{day}) < 2.9$ using α_{LSP} and β_{LSP} . We subsequently calculate the distance moduli and the luminosity distances. The uncertainty of the luminosity distances is caused by the propagated *Gaia* period uncertainty and the intrinsic scatter of the P - M_{JKs} relation using the uncertainty in the fitted PLR. We neglect the difference between O-rich and C-rich OSARGs, as there is no obvious distinction in their P - M_{JKs} sequences, and the majority ($\sim 97\%$) of stars in our sample are O-rich LPVs according to the *is_cstar* label in the *Gaia* LPV catalogue (Lebzelter et al. 2023). Sanders & Matsunaga (2023) show that the *is_cstar* label classifies highly extinguished stars as C-rich, which means the true fraction of O-rich stars is even higher than 97%. We have also inspected the metallicity dependence of the period- M_{JKs} relation and treat this as a second-order effect (Zhang et al. in prep.).

We cross-validate the luminosity distances with various catalogues that have distances, including parallax-based geometric distances (Bailer-Jones et al. 2021), spectroscopic StarHorse distances (Queiroz et al. 2020), and distances to globular cluster members (Vasiliev & Baumgardt 2021). For the geometric distances, we cut the comparison sample to select stars with small fractional parallax uncertainties, i.e. $\sigma_{\varpi}/\varpi < 0.1$. We focus on the comparison with the geometric distances and StarHorse distances as they have a sufficient number of cross-matches with our data. Stars with distance modulus uncertainties greater than 0.4 (roughly corresponding to $\sim 20\%$ distance uncertainties) are removed from our sample, which removes stars with large period uncertainties. In Fig. 2, we plot the luminosity distances versus the reference distances from the other catalogues in the upper panel and the ratio between the two distances versus the reference distances in the lower panel. The grey dashed lines represent the 1:1 line. Overall, we demonstrate a good 1:1 correlation between the assigned luminosity distances and the distances calibrated using various other methods. For the geometric and StarHorse distances, we take bins of the reference distances and compute the median of the distance ratio in each bin. We plot the median of the distance ratios as the red and blue lines, respectively, for the geometric and StarHorse distances. For the comparison with the geometric distances, the median ratio is consistent with the 1:1 lines at small distances and deviates at large distances, as expected for the parallax-based distances. The lower panel of Fig. 2 reveals that the luminosity distances agree with the other distance calibrations with only $\sim 5\%$ deviation.

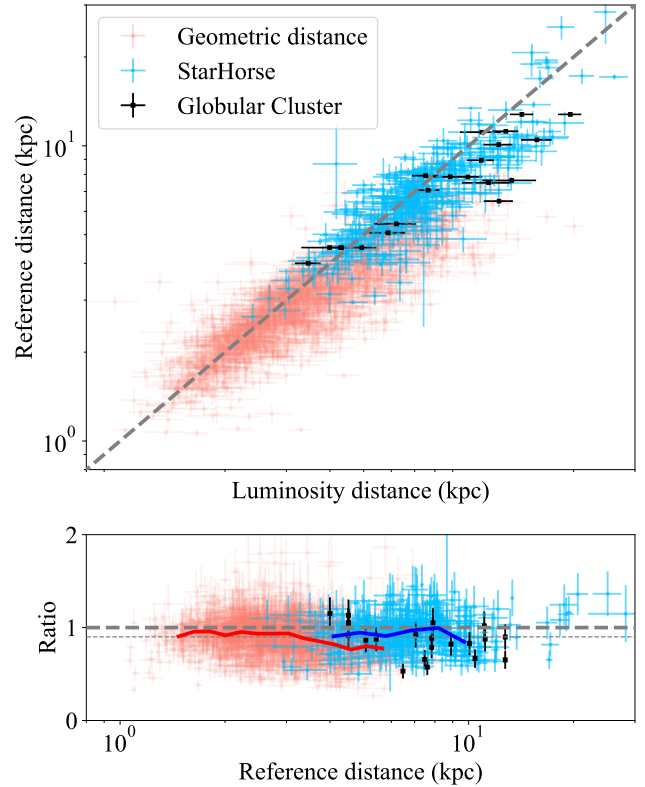


Figure 2. We compare the luminosity distances of stars we assigned in this work to other samples with calibrated distances using various methods. We represent the cross-match with the parallax-based geometric distances in Bailer-Jones et al. (2021) as red, spectroscopic StarHorse distances in Queiroz et al. (2020) as blue, and globular cluster members from Vasiliev & Baumgardt (2021) as black dots. In the upper panel, we show the distances of stars from other catalogues on the x-axis and the luminosity distances on the y-axis. The grey dashed line represents the 1:1 line. The lower panel shows the reference distances from other methods versus the ratio between the reference distances and luminosity distances. The thick grey line is the 1:1 line, while the thinner line below shows the 90% consistency (1:0.9 line). The red and blue lines are the median distance ratio when using the geometric distances and StarHorse distances as references. We argue that the assigned luminosity distances are $\sim 95\%$ consistent with those reference distances.

2.4 Final sample

We summarise the quality cuts applied to the *Gaia* LPV catalogue below. We crossmatch *Gaia* LPV SOS table to 2MASS for infrared photometry, and we remove stars without good JHK_s photometry by requiring `ph_qual = AAA` and remove galaxy contamination by requiring `gal_contam = 0`. We remove potential YSO contamination using `best_class_score > 0.8`. We retain stars only if the *Gaia* published period is between $1.6 < \log(P[\text{days}]) < 1.9$ or $2.4 < \log(P[\text{days}]) < 2.9$ and G amplitude < 0.15 to select LA-LPV candidates. After assigning the luminosity distances, we remove stars with magnitude uncertainties greater than 0.4, i.e. $\sigma_M < 0.4$, corresponding to cutting at $\sim 20\%$ fractional distance uncertainty. This effectively cuts on the period uncertainty as the intrinsic scatter of the P - M_{JKs} relation is fixed. The published *Gaia* period uncertainties associated with the LSP sequence are large, and thus, only a few stars on that sequence survive the magnitude uncertainty cut. Over 98% of stars in the final sample have their luminosity

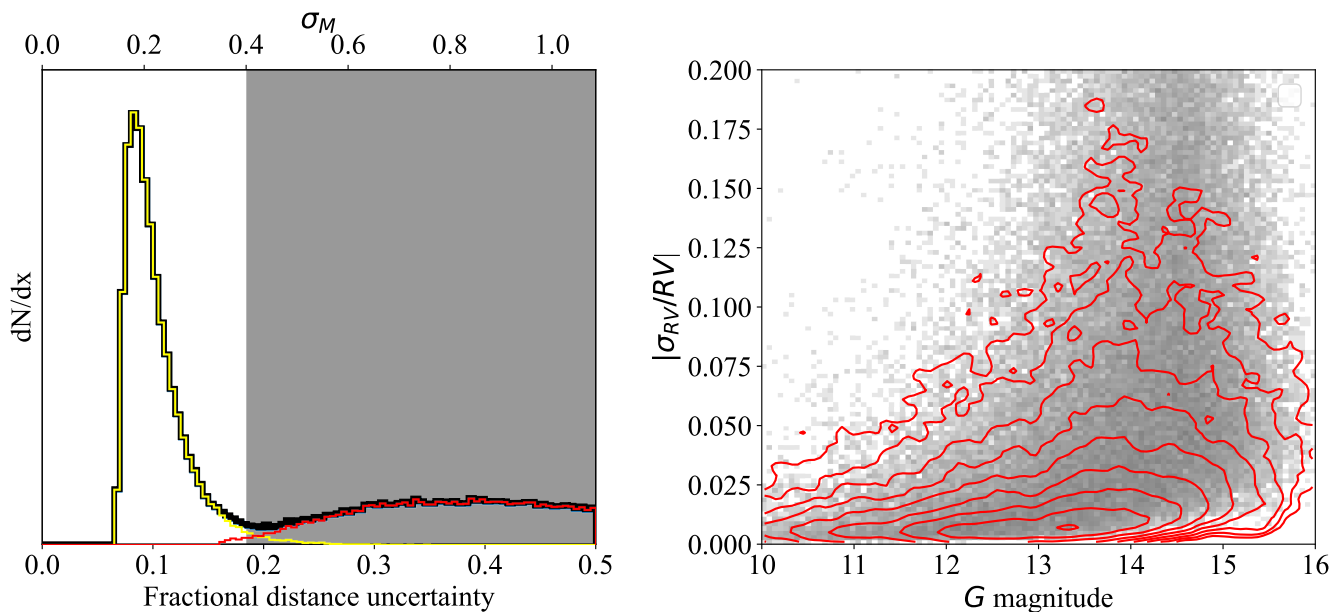


Figure 3. We show the fractional distance uncertainty distribution of the sample in the left panel, where the corresponding uncertainty in the absolute magnitude uncertainty is shown on the top x-axis. The yellow and red lines are the distance uncertainty for OSARGs and LSP, and the black line is the distance uncertainty distribution for the sample overall. We cut the final sample at $\sigma_M < 0.4$, corresponding to $\sim 18\%$ distance uncertainty. The removed region is masked in grey. In the right panel, we compare the fractional radial velocity uncertainty in our final sample (red contours) to a randomly selected *Gaia* sample (black 2D histogram). We argue the *Gaia* radial velocity measurements of these LA-LPVs are faithful due to the similarity of their distribution to the randomly selected *Gaia* sample.

distances assigned using OSARG’s period-luminosity sequence because the period uncertainties associated with LSP candidates are large. There are 45,819 stars left. In the left panel of Fig. 3, we show the distribution of the fractional distance uncertainties of this sample. The mean and median distance uncertainty of this sample is $\sim 10\%$. To perform kinematic and dynamical analysis, we further remove stars without radial velocity measurements from *Gaia* DR3. This leaves a final sample size of 33 704 stars.

To validate the radial velocity measurements for this LA-LPV sample, we compare the fractional radial velocity uncertainty, $|\sigma_{RV}/RV|$, to a randomly selected *Gaia* sample with radial velocity measurements. We randomly select 100 000 stars from *Gaia* with radial velocity measurements, and we crossmatch it to the sample constructed above and remove common stars. In the right panel of Fig. 3, we plot the fractional radial velocity uncertainty against *G* magnitude. The background shows the distribution of the randomly selected *Gaia* sample, and the red contours are the distribution of our sample. We illustrate that the small variability of stars in this sample does not affect the radial velocity measurement from *Gaia* as both samples share a similar distribution.

We show the on-sky (ℓ and b) distribution and the spatial coverage of the final sample in Fig. 4. Most stars reside below $|b| \sim 25^\circ$ and $|z| \sim 2.5$ kpc, where R and z are the Galactocentric cylindrical coordinates. The sample traces the Milky Way from the centre out to $R \sim 15$ kpc, showing complete coverage of the inner Milky Way. Some of these stars have large luminosity distances extending to the other side of the Galaxy. The face-on view of the Galactic disc shows an overdensity compatible with the shape and orientation of the Galactic bar, giving us a unique opportunity to view the entire bar and study the kinematics of stars on the other side of the bulge.

2.5 Selection effects

Because our selection of LA-LPV candidates is based purely on photometry and given the full-sky coverage of *Gaia*, the LA-LPV sample has no sharp truncation in the spatial map. This allows us to present a panoramic map of the inner Galaxy and study the kinematics and dynamics homogeneously. The LA-LPV and SRV candidates in OGLE-BLG compiled by Soszyński et al. (2013) and analysed in Hey et al. (2023) has a larger sample size than our sample because OGLE has deeper photometry than *Gaia* and also has a higher recovery rate of LPV candidates. However, due to the limited footprint of the OGLE-BLG survey (Soszyński et al. 2013), the selection function has a large spatial variation. Compared to OGLE, except for the incompleteness in star counts within $|b| < 2^\circ$ due to the dust extinction as shown in the top panel of Fig. 4, in our sample, the observational footprint does not impose extra spatial variation in the selection function.

In addition to the selection function caused by the extinction, there is a selection function in the apparent magnitude caused by the radial velocity cut. To the first order, this can be approximated as an absolute magnitude cut that changes with the distance from the Sun. However, due to the high intrinsic luminosity of LPVs ($M_{JKs} \lesssim -6$) as well as the period and amplitude cuts applied, we limit the absolute magnitude to $-8 \lesssim M_{JKs} \lesssim -7$ for stars in our sample. This limit has the effect that a similar population of stars is selected at all heliocentric distances, except for stars that are very close (heliocentric distance $\lesssim 2$ kpc, where the observation is saturated) or very far (heliocentric distance $\gtrsim 12$ kpc, where stars are too faint to have radial velocity measurements). Therefore, the selection function in magnitude does not cause spatial variation on the number of selected stars as a function of heliocentric distances, to the first order.

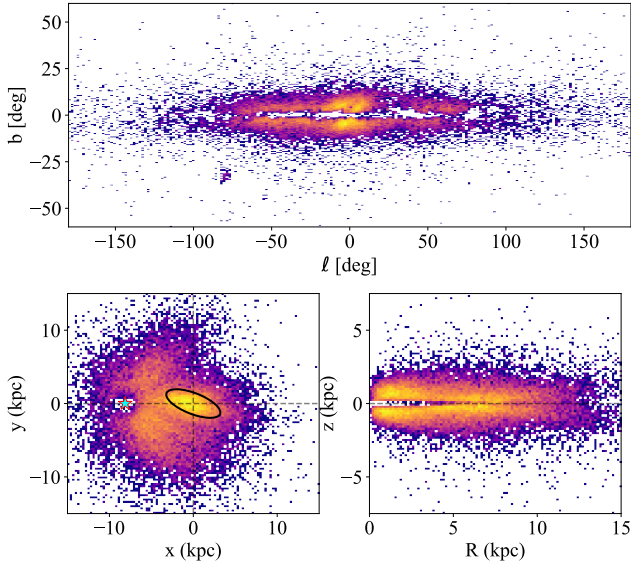


Figure 4. The upper panel shows the on-sky view of the sample in terms of the Galactic longitude and latitude, ℓ and b . The lower left panel is the face-on view of the sample in Galactocentric Cartesian coordinates. The Sun is located at $x = -8.122$ kpc and is labelled by the aqua star. The Galactic bar is drawn with the black ellipse and is assumed to orient 25° , leading the Sun. The lower right panel shows the Galactocentric cylindrical distribution of the sample.

3 KINEMATICS OF THE GALACTIC BAR

To focus on the inner Galaxy, we only keep stars with $|x| < 5$ kpc and $|y| < 5$ kpc. With the full 6D phase space measurements of $\sim 20\,000$ stars in the inner Milky Way, we map their kinematics. We derive the positions and velocities in Galactocentric Cartesian coordinates and right-handed cylindrical coordinates from astrometric and radial velocity measurements from *Gaia* DR3 and use the assigned luminosity distances instead of parallax. The location of the Sun is $x = -8.122$ kpc, and the solar velocities are (12.9, 245.6, 7.78) km/s in the radial, azimuthal, and vertical directions, respectively (Schönrich et al. 2010). The uncertainties are propagated using the Monte Carlo method. In this section, we analyse the kinematics of this sample and use N-body simulation results as references to calibrate the parameters of the Galactic bar.

3.1 Velocity fields

We employ the approach from Gaia Collaboration et al. (2023b) by binning the stars into pixels in the $x - y$ plane. Inside each pixel, we estimate the mean velocity \bar{V}_i and velocity dispersion σ_i^* of the velocity component $i \in (R, \phi, z)$ by deconvolving the measurement uncertainty for each star in the pixel. We write the log-likelihood as

$$\ln L(\bar{V}_i, \sigma_i^*) = -\frac{1}{2} \sum_j^N \left[\ln(\sigma_i^{*2} + \sigma_{i,j}^2) + \frac{(v_{i,j} - \bar{V}_i)^2}{\sigma_i^{*2} + \sigma_{i,j}^2} \right], \quad (3)$$

where $v_{i,j}$ and $\sigma_{i,j}$ are the i -component velocity of j th stars in the pixel, and N is the total number of stars in the pixel. We minimise the negative log-likelihood using the Nelder-Mead method in `scipy`. We separate stars into 400×400 pc² squares in the $x - y$ plane and compute the mean velocity and velocity dispersion in cylindrical components R , z , and ϕ for each pixel.

The radial component of the velocity is particularly interesting when studying the kinematics of the bar. We show the mean radial velocity and radial velocity dispersion in the middle row in Fig. 5. The quadrupole pattern around the Galactic centre (GC) in the mean radial velocity map is a common signature of bars seen in cosmological simulations (Fragkoudi et al. 2020) and in MW observations (Bovy et al. 2019; Queiroz et al. 2021; Leung et al. 2023; Gaia Collaboration et al. 2023b; Liao et al. 2024). The pattern is caused by the streaming motion and the elongated orbits of the bar-supporting stars. The quadrupole pattern should be aligned with the major axis of the bar, but it aligns more with the line joining the Sun and the Galactic centre in our data. This effect arises because the heliocentric distance uncertainty blurs a star's observed position along the line-of-sight from its true location. This elongates the bar and biases its orientation. The effect of the uncertainty is analysed using N-body simulations in the literature (Vislosky et al. 2024; Hey et al. 2023). We will also calibrate it later in our N-body simulation. Recently, Hey et al. (2023) studied the kinematics of the Galactic bulge using the same tracer, LA-LPVs, in the OGLEIII-BLG survey (Soszyński et al. 2013). They show the same mean radial velocity pattern, which also extends to the other side of the disc. The bisymmetric feature in the radial velocity dispersion with the node residing on the Galactic centre also agrees with results in Gaia Collaboration et al. (2023b).

In the bottom panels of Fig. 5, we present the mean \bar{V}_z , and \bar{V}_ϕ maps. The mean vertical velocity shows no systematic patterns on both sides of the bar, meaning that it is vertically stable at the present day. The mean azimuthal velocity drops quickly when approaching the Galactic centre, as expected from e.g. Leung et al. (2023). The contours of the mean azimuthal velocity map should align with the major axis of the bar in an error-free case, but the heliocentric distance uncertainty in our sample biases the contours to align with the Sun-GC line.

We define the mean radial fraction of the total velocity as

$$\left\langle \left| \frac{v_R}{v_{\text{tot}}} \right| \right\rangle = \frac{1}{N} \sum_j^N \frac{|v_{R,j}|}{v_{\text{tot},j}}, \quad (4)$$

where $v_{\text{tot},j}$ is the total velocity of j th star in the pixel. The $\langle |v_R/v_{\text{tot}}| \rangle$ map is shown in the top right panel of Fig. 5. As the x_1 orbits considered the backbone of the Galactic bar (Patsis & Athanassoula 2019; Petersen et al. 2021), are dominated by the radial motion, the region that is well-populated by x_1 orbits should have high $\langle |v_R/v_{\text{tot}}| \rangle$. This makes the mean radial velocity fraction map a good tracer of the extent of the bar's x_1 orbits and hence the Galactic bar itself. As expected, $\langle |v_R/v_{\text{tot}}| \rangle$ becomes higher closer to the centre, and the shape and orientation of the contours agree with a hypothetical bar that is inclined 25° above the x -axis, as shown by the black dashed ellipse. Inspired by the prominent patterns in these kinematic projections, we conclude that the bar stars are a prominent population in our sample on both sides of the Galaxy. The full sky coverage of the *Gaia* sample helps to mitigate the selection effects compared to the sample in e.g. Hey et al. (2023) and enables further quantitative analysis.

3.2 N-body Simulation

We present below the setups and the results of two Milky Way-analogue N-body simulations. In both cases, the Galactic bar forms within 2 Gyr after the beginning of the simulation. We only run the N-body simulations to test the methodology and to understand the impact of distance uncertainties and the selection function. Ac-

Data

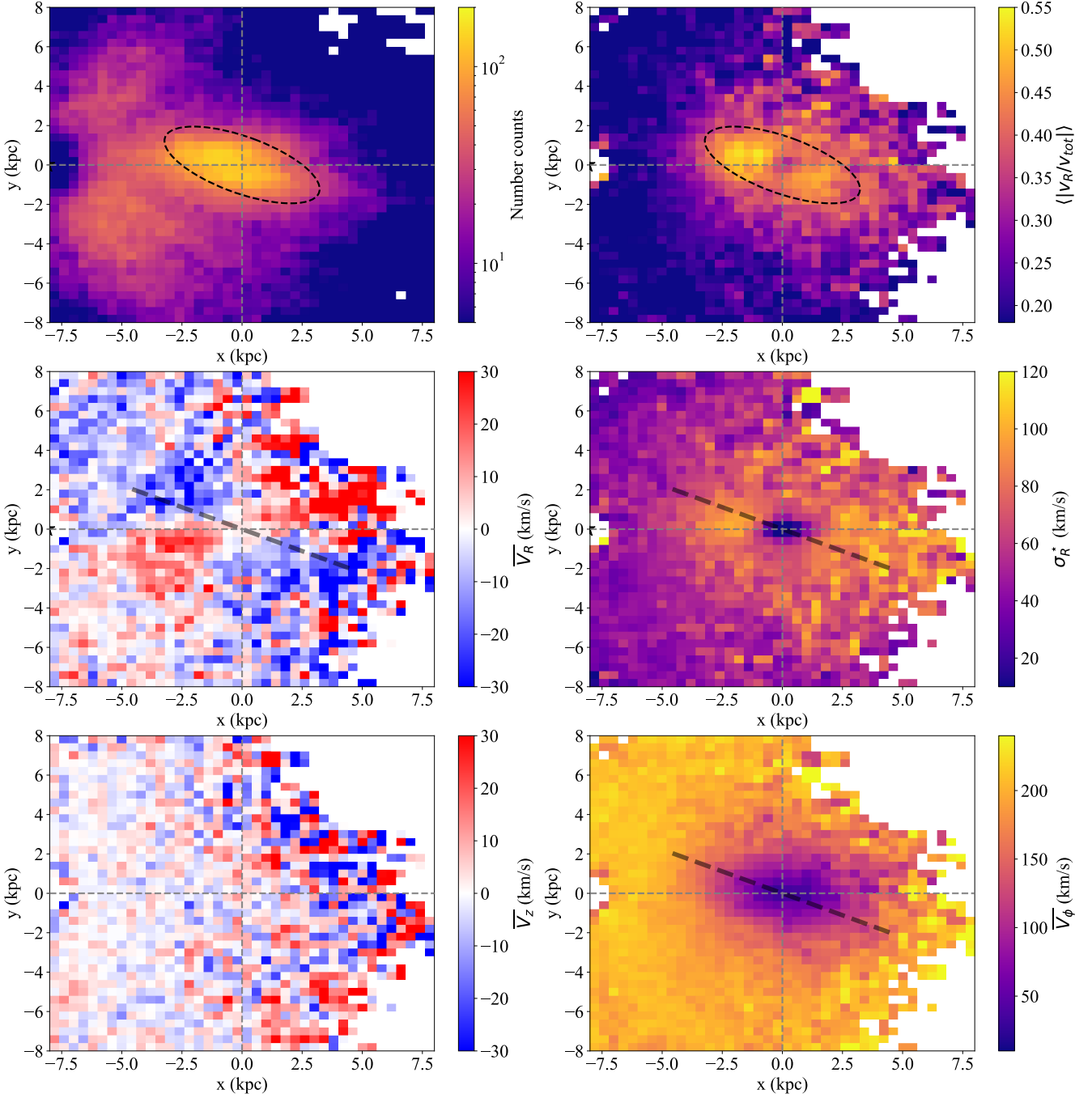


Figure 5. We present a set of kinematic maps of stars in our sample. In the top row, the left panel shows the stellar density and the right panel maps the mean radial fraction of total velocity. The black ellipse follows the orientation of the bar in this coordinate. The middle panels show the mean radial velocity and radial velocity dispersion. The bottom panels are the mean vertical and azimuthal velocity maps, respectively. For the middle and bottom panels, the mean velocity and dispersion are computed accounting for measurement uncertainties by minimising the negative log-likelihood in Eq. 3.

cordingly, we focus on the initialisation and basic properties of the snapshots here.

3.2.1 Galaxy A

The simulated galaxy has four main components: a stellar disc, a gaseous disc, a classical bulge and a halo. The stellar disc is composed of a thin and thick disc; the halo includes both dark matter and the stellar halo. An equilibrium, self-consistent model

of these components is generated using the AGAMA (Vasiliev 2019) self-consistent model routine. In brief, the program provides initial conditions using action-based distribution functions in a Milky Way-like potential. Given an initial guess of the galactic potential, a density distribution is computed by calculating the zeroth-order velocity moment of the distribution functions. The distribution function is updated with the new potential from the generated density distribution, but the action-based functional form remains unchanged throughout the routine. We iterate the last two steps until they converge. A more detailed description and justification of the procedures is in Vasiliev (2019) (also see Tepper-Garcia et al. 2021).

We employ the quasi-isothermal distribution function in Eq. 5 for the disc-like structures (Binney 2010) and the double-power law form in Eq. 6 that is similar to Posti et al. (2015) and Williams & Evans (2015) for the spheroidal-like structures. The distribution function parameters we used to generate the initial conditions of the N-body simulation are given in Tables 1 and 2, where the parameters listed follow the same definition as in Eq. 5 and 6. Parameters not shown in the Tables are set to their default AGAMA (1.0 version) values. The initial potential is the best-fit potential from McMillan (2017), though the choice of the initial potential only weakly affects the final self-consistent model. After the iteration as described above, in the self-consistent model, the total mass of the disc is $\sim 4.6 \times 10^{10} M_\odot$; the halo $\sim 1.1 \times 10^{12} M_\odot$; the bulge $\sim 9.0 \times 10^9 M_\odot$, which are all consistent with the value estimated for the Milky Way (Bland-Hawthorn & Gerhard 2016). The radial scale length of the disc, R_d , is ~ 2.5 kpc. The mass of the static gaseous disc is set to $\sim 10^{10} M_\odot$.

The detailed DFs for disc and halo are given for completeness:

$$f(\mathbf{J}) = \frac{\tilde{\Sigma} \Omega}{2\pi^2 \kappa^2} \times \frac{\kappa}{\tilde{\sigma}_r^2} \exp\left(-\frac{\kappa J_r}{\tilde{\sigma}_r^2}\right) \times \frac{\nu}{\tilde{\sigma}_z^2} \exp\left(-\frac{\nu J_z}{\tilde{\sigma}_z^2}\right) \times B(J_\phi),$$

$$B(J_\phi) = \begin{cases} 1 & \text{if } J_\phi \geq 0, \\ \exp\left(\frac{2\Omega J_\phi}{\tilde{\sigma}_\phi^2}\right) & \text{if } J_\phi < 0, \end{cases},$$

$$\tilde{\Sigma}(R_c) \equiv \Sigma_0 \exp(-R_c/R_{\text{disc}}),$$

$$\tilde{\sigma}_r^2(R_c) \equiv \sigma_{r,0}^2 \exp(-2R_c/R_{\sigma,r}) + \sigma_{\text{min}}^2,$$

$$\tilde{\sigma}_z^2(R_c) \equiv 2h_{\text{disc}}^2 \nu^2(R_c) + \sigma_{\text{min}}^2, \quad (5)$$

$$f(\mathbf{J}) = \frac{M}{(2\pi J_0)^3} \left[1 + \frac{J_0}{h(\mathbf{J})}\right]^\Gamma \left[1 + \frac{g(\mathbf{J})}{J_0}\right]^{-\beta} F(J_{\text{cut}}),$$

$$F(J_{\text{cut}}) \equiv \exp\left[-\left(\frac{g(\mathbf{J})}{J_{\text{cut}}}\right)^2\right],$$

$$h(\mathbf{J}) \equiv h_r J_r + h_z J_z + (3 - h_r - h_z) |J_\phi|,$$

$$g(\mathbf{J}) \equiv g_r J_r + g_z J_z + (3 - g_r - g_z) |J_\phi|, \quad (6)$$

The initial conditions for the N-body simulation are sampled using the AGAMA sampling routine. We evolve the particles using PyFALCON, the Python interface of FALCON code (Dehnen 2000), for 6 Gyr. The softening length is set to 25 pc, and the timestep is 0.122 Myr. A snapshot is taken for every 0.25 Gyr, and for every time, a consecutive snapshot is taken at 15 Myr later to calculate the pattern speed of the bar using the finite difference method. The fraction of disc to total mass enclosed in $2.2 \times R_d$ is $f_d \sim 0.6$. This factor is a good indicator of bar instability—in particular, the bar formation timescale is shorter for larger f_d (Fujii et al. 2018). If $f_d \sim 0.6$, then the bar formation timescale is well below a Hubble

time. A bar formed within 1 Gyr in our simulation. We save all the snapshots after 1 Gyr from the start of simulation for later analysis. The pattern speeds of all the saved snapshots in simulated Galaxy A lie between $\sim 12 - 32 \text{ km s}^{-1} \text{ kpc}^{-1}$. We focus on the snapshot at 2 Gyr as a representative example of Galaxy A to analyse the bar kinematics therein.

In the snapshot at 2 Gyr after the beginning of the simulation, the rotation curve is $\sim 210 \text{ km/s}$ at the Sun. The pattern speed, Ω_b , is $27 \text{ km s}^{-1} \text{ kpc}^{-1}$ calculated with the finite difference method. The bar angle and bar length in each snapshot are computed using the Fourier monopole and quadrupole components:

$$A_m(R) = \frac{1}{\pi} \int_0^{2\pi} \Sigma(R, \phi) \cos(m\theta) d\theta,$$

$$B_m(R) = \frac{1}{\pi} \int_0^{2\pi} \Sigma(R, \phi) \sin(m\theta) d\theta,$$

and the bar strength A_b and angle, ϕ_b , can be written as

$$A_b(R) \equiv \sqrt{A_2^2 + B_2^2}/A_0, \quad (7)$$

$$\phi_b = \frac{1}{2} \tan^{-1}(B_2/A_2), \quad (8)$$

respectively. Similar to Rosas-Guevara et al. (2022), we define the bar half-length R_b as the radius which $A_b(R_b) = 0.15$, and the bar half-length is then ~ 5.8 kpc.

3.2.2 Galaxy B

We supplement the simulated galaxies by another N-body simulation, which we adopt from Tepper-Garcia et al. (2021). Tepper-Garcia et al. (2021) present a three-component Milky Way-analogue galaxy that is constituted by a stellar bulge, a stellar disc, and a dark matter halo. We reproduce the N-body simulation in Tepper-Garcia et al. (2021) using the same parameters. While the disc is initialised with the quasi-isothermal distribution (Eq. 5) and corresponding parameters therein, the bulge and dark matter halo's distribution functions are initialised directly from their defined density distribution using QuasiSpherical method in AGAMA that builds on the Eddington inversion formula. The resulting self-consistent model has a disc with mass $\sim 4.4 \times 10^{10} M_\odot$, a bulge with $\sim 1.3 \times 10^{10} M_\odot$, and a halo with mass $\sim 1.7 \times 10^{12} M_\odot$. No gaseous disc is set in this simulation.

We run the N-body simulation with the same code and parameters as the previous model. We also take snapshots with the same time step and simulate 6 Gyr. The bar settles in this simulation within ~ 1.5 Gyr. Hence, we save all snapshots afterwards. The pattern speeds of the bar in this simulation setup resides in the range between $30 - 45 \text{ km s}^{-1} \text{ kpc}^{-1}$, measured using the finite difference method. Similar to Galaxy A, we choose the snapshot at $t = 4$ Gyr to represent Galaxy B. The pattern speed of the bar in this snapshot is $32.56 \text{ km s}^{-1} \text{ kpc}^{-1}$, similar to that of the Milky Way.

3.3 Kinematics of Galaxy A

In a similar way to the handling of the data, we plot the kinematics of Galaxy A by binning stars in pixels in the $x - y$ plane as shown in Fig. 6. We rotate Galaxy A so that the major axis of the bar also inclines 25° ahead of the x -axis to mimic the Milky Way. A clear quadrupole pattern is observed in the mean radial velocity map of

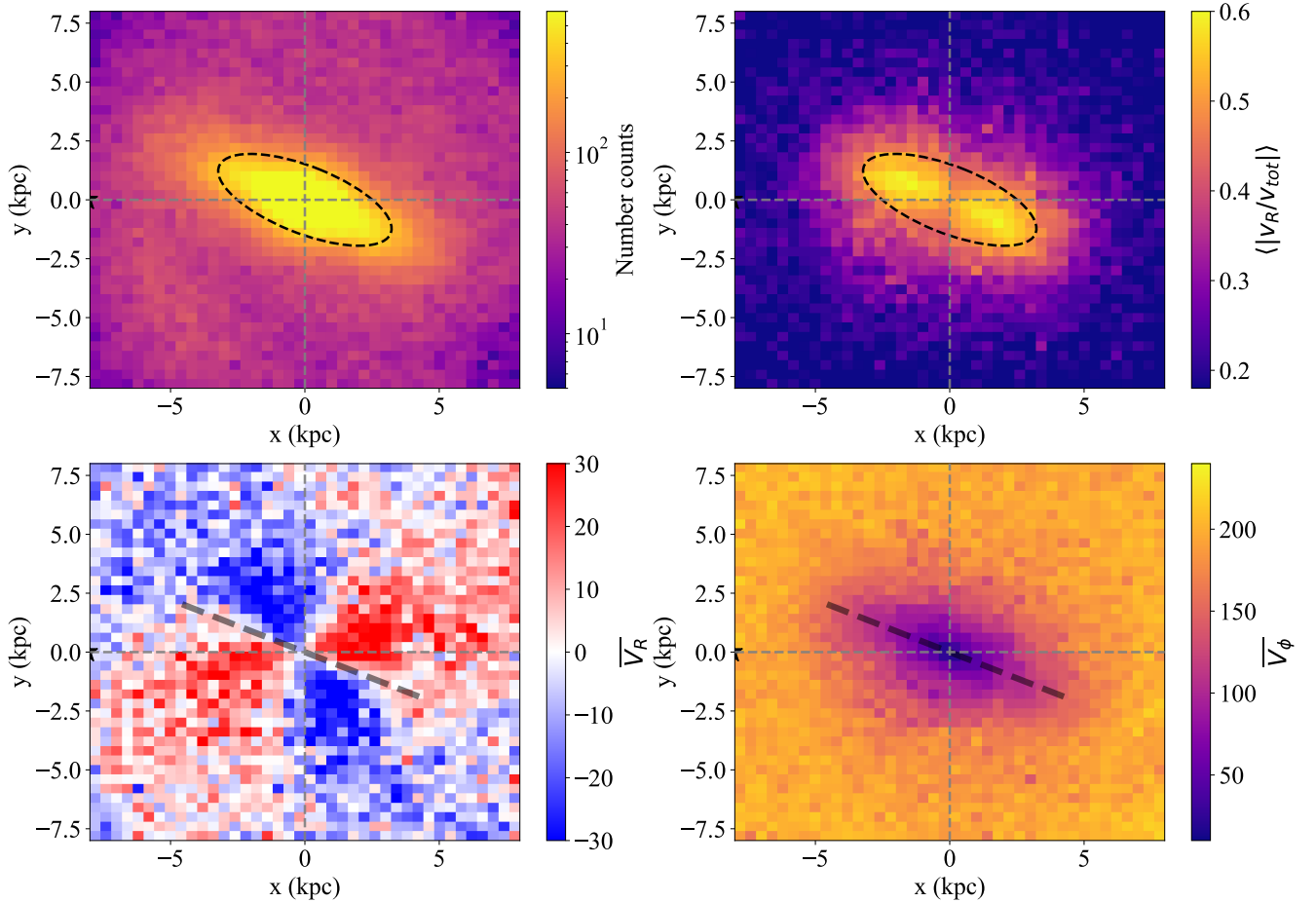
Table 1. Quasi-isothermal distribution function parameters for disc-like components. The definition of parameters follows Eq. 5.

Components	Σ_0 ($\times 10^8 M_\odot \text{kpc}^{-2}$)	R_{disc} (kpc)	h_{disc} (kpc)	$\sigma_{r,0}$ (km/s)	σ_{min} (km/s)	$R_{\sigma,r}$ (kpc)
Thin disc	8.9	2.5	0.2	100	5.0	6.0
Thick disc	1.8	3.0	0.6	180	5.0	6.0

Table 2. Double exponential distribution function parameters for spheroidal-like components. The definition of parameters follows Eq. 6.

Components	M ($\times 10^9 M_\odot$)	Γ	β	J_0 (kpc km/s)	h_r	h_z	g_r	g_z	J_{cut} (kpc km/s)
Bulge	0.03	0	1.8	2.0	1.4	0.8	1.4	0.8	280
Stellar halo	1.5	0	3.5	500	-	-	1.6	0.7	100,000
Dark matter halo	4,000	1.2	3.1	16,000	1.4	0.8	1.2	0.9	20,000

(Simulated) Galaxy A


Figure 6. The stellar density (upper left), radial velocity (lower left), azimuthal velocity (lower right) and the mean radial fraction of the total velocity (upper right) map of the simulated Galaxy A is shown in this figure. We do not show the map of σ_R^* and V_z as they are less interesting. The line and ellipse contour are both inclined 25° above the x-axis to denote the orientation of the bar in this galaxy.

Galaxy A as shown in the lower left panel in Fig. 6. The same quadrupole pattern is seen in other simulated barred galaxies. As shown in the top right panel in Fig. 6, the value of $\langle |v_R/v_{\text{tot}}| \rangle$ is high in the bar region as expected due to the orbital structures of the bar-supporting stars.

To fairly compare the simulation with observations, we repeat the analysis in Hey et al. (2023) and Vislosky et al. (2024). We scatter the particles in Galaxy A with heliocentric distance uncertainties and investigate how this propagates to the kinematics. We neglect the proper motion and radial velocity uncertainty in this analysis as they are less significant than the distance uncertainty. The top row of Fig. 7 shows the stellar density map of Galaxy A with different heliocentric distance uncertainties. The heliocentric distance uncertainties blur the shape of the bar as expected. By smearing the position of the stars along the line-of-sight direction, the bar is artificially stretched and biased towards the Sun-GC line. In the middle panel of Fig. 7, we present the mean radial velocity field of Galaxy A in different fractional heliocentric distance uncertainties. The black dashed line shows the orientation of the true major axis of the bar, and in an error-free galaxy, the quadrupole pattern changes signs when crossing the major axis of the bar. However, in the presence of 20% heliocentric distance uncertainty, the sign-switching position changes from the true major axis of the bar to the Sun-GC line. We also find the $\langle |v_R/v_{\text{tot}}| \rangle$ map is less affected by the heliocentric distance uncertainty as shown in the bottom panels. While the $\overline{v_R}$ map has sign-switching along with the Sun-GC line, the orientation of the $\langle |v_R/v_{\text{tot}}| \rangle$ map is less biased and still preserves the original angle of the bar as shown by the white contour. Hence, we argue that we can use the signal in the measured $\langle |v_R/v_{\text{tot}}| \rangle$ map to estimate the angle of the bar. Although the distance uncertainty still bends the true major axis to the Sun-GC line, the velocity ratio is less affected by the distance uncertainty compared to the radial velocity. Therefore, the overall contribution from the distance uncertainty is less in the $\langle |v_R/v_{\text{tot}}| \rangle$ map than the mean radial velocity map.

We further apply the selection function of our data to Galaxy A to mimic the observation. The selection function is implemented by selecting and retaining the closest mock particle in the Cartesian coordinate to an observed star. We discard simulated particles that either fail to become a closest match in xyz or for which the distance between the real star and the closest-matched mock particle is greater than 0.1 kpc. After matching the selection function, the simulated stars have roughly the same number counts as the dataset while also mimicking the spatial distribution. In the rightmost column of Fig. 7, we show the kinematics of Galaxy A after scattering particles by 10% distance uncertainty and applying the selection function. In the top right panel, the stellar density map, after applying the selection function, is identical to that in Fig. 5 by design. We highlight the similarities compared to the kinematics of our dataset in Fig. 5. Testing the robustness of these kinematic maps by adding $\sim 5\%$ systematic distance bias, we conclude that the maps are qualitatively the same with a minor distance bias. This reinforces the validity of our sample uncertainties and analysis while also demonstrating the power of this sample in studying the Galactic bar.

3.4 A kinematic measurement of the Galactic bar length

The length of the galactic bar is usually defined through the stellar overdensity or the apocentre of bar-supporting stars (Athanasoula & Misiriotis 2002; Petersen et al. 2021; Lucey et al. 2023). Athanasoula & Misiriotis (2002) proposed finding the bar length by elliptical fitting. The Fourier quadrupole mode is also frequently used

to define the bar length. The radius at which the bar strength, A_b in Eq. 7, falls below some threshold (20% of the maximum value in A_b is adopted for the threshold in Athanasoula & Misiriotis 2002). The bar length varies when different thresholds are chosen (Athanasoula & Misiriotis 2002; Rosas-Guevara et al. 2022). Also, Hilmi et al. (2020) showed that the bar length estimates using these methods are biased when a spiral arm connects to the bar. The dynamical length defined by the extent of the bar-supporting stars' orbits is less affected by the connected spiral arm (Petersen et al. 2024).

Detecting bar-supporting orbits is usually done either by selecting stars through orbital frequency ratios (Portail et al. 2015b; Lucey et al. 2023) or through a rigorous algorithm to find the x_1 orbits (Petersen et al. 2021). In either case, the classification requires knowledge of the gravitational potential in the inner Galaxy, as we need to integrate the orbits to know the orbital families. However, as the signature of bar orbits is likely the cause of the high-value signal in the $\langle |v_R/v_{\text{tot}}| \rangle$ map, we explore the possibility of using the $\langle |v_R/v_{\text{tot}}| \rangle$ map to define the dynamical length of the bar. This is similar to the method in Petersen et al. (2024), which uses the mean v_{\perp} map to detect the oscillation in the x_1 orbits, where v_{\perp} is the velocity in the direction perpendicular to the bar major axis. Petersen et al. (2024) used the ratio of the octupole and quadrupole moment of the mean v_{\perp} map to track the extent of the x_1 orbits. However, as the method involves knowledge of higher-order Fourier components, it is necessary to have full coverage and high signal-to-noise ratio measurements in the inner Galaxy. Therefore, the method is more suitable for simulations and extragalactic observations than for applications to the Milky Way.

To test the hypothesis that the signal in $\langle |v_R/v_{\text{tot}}| \rangle$ is due to the nature of the bar orbits, we turn to our simulations. The $\langle |v_R/v_{\text{tot}}| \rangle$ map of Galaxy A and B are presented in the top left and middle panel in Fig. 8. To classify the orbits, we use the multipole expansion method implemented in AGAMA to obtain the potential of the snapshot, and then we integrate the particles for 2 Gyr. The pattern speed of the potential is again calculated using the finite difference method. For each particle, we compute the Fast Fourier Transform (FFT) of the time series in R and X coordinates and find the primary peaks as the orbital frequencies, where X is aligned with the major axis of the bar. We denote Ω_i as the orbital frequency in the i -axis. The distinction between a bar and a disc particle is simple in practice. We use a similar cut as Portail et al. (2015b) and assign stars with $\Omega_R/\Omega_X \in 2 \pm 0.2$ and $r_{\text{apo}} < 7$ kpc to the bar, where r_{apo} is the spherical apocentric radius of the orbits. Although cutting on the apocentric radius conflicts with the purpose of this test, the resulting extent of bar orbits is far smaller than 7 kpc. We only use this cut to remove the disc contamination that has an orbital frequency ratio satisfying the bar selection by coincidence. The contours of the distribution of selected bar stars are shown in the top and middle panels of Fig. 8 in white. The distribution of the bar stars matches beautifully to the shape of the signal in the $\langle |v_R/v_{\text{tot}}| \rangle$ map, reinforcing the idea that it can be used as a kinematic tracer of bar orbits.

Additionally, for these selected bar stars, we run a selection of x_1 orbits. We apply the method proposed in Petersen et al. (2021). As a short summary of the method, the x_1 orbits are selected by examining the spatial compactness of the apocentre distribution at the two ends of the bar for each trajectory. The 2D spatial information of 20 consecutive apocentres is recorded for each trajectory, and the k-mean clustering method (Lloyd 1982, $k = 2$ corresponding to two ends of the bar) is employed to assess the compactness of these apocentres relative to the ends of the bar. The expected purity

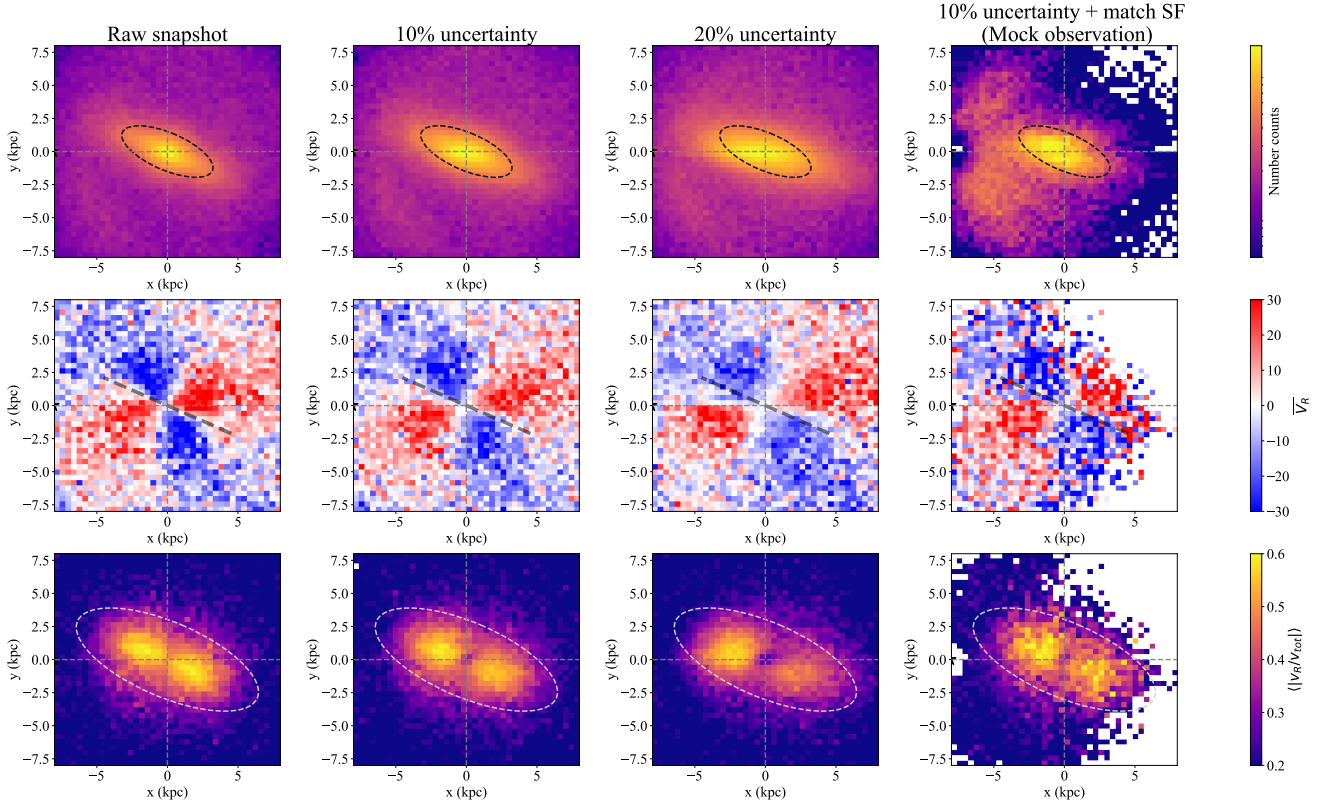


Figure 7. We present the effect of the heliocentric distance uncertainty and selection function on the kinematics maps by applying them to *simulated* Galaxy A. In the leftmost column, we show raw stellar counts of Galaxy A and its kinematics that are free of uncertainty and have 100% completeness. The middle columns show Galaxy A after scattering the particles by 10% and 20% heliocentric distance uncertainty. The rightmost column shows Galaxy A after scattering with 10% distance uncertainty and matching with the selection function (SF) of the dataset, which gives a suitable mock representation of the observation. The black dashed lines and ellipse contour in each panel are used to label the true bar angle.

of x_1 orbits selected using this method is $\sim 99\%$ (Petersen et al. 2021), but we also visually inspected all of the selected x_1 orbits to ensure the algorithm performs as expected. The bar lengths estimated from the radius spanned by x_1 orbits, denoted as R_{x_1} , are 5.5 and 4.1 kpc for Galaxies A and B and are labelled by the vertical grey dashed line in the corresponding panel in Fig. 8. R_{x_1} agrees with the outskirts of $\langle |v_R/v_{\text{tot}}| \rangle$ signal in both simulated galaxies. In the bottom panels of Fig. 8, we show the $\langle |v_R/v_{\text{tot}}| \rangle$ value as a function of radius along the major axis of the bar in red solid lines. The vertical dashed line again labels R_{x_1} , and in both galaxies corresponds to $\langle v_R/v_{\text{tot}} \rangle \approx 0.3$. Hence, we use $\langle v_R/v_{\text{tot}} \rangle|_{R_b} = 0.3$ as a kinematic estimation of the bar length that is calibrated to agree with R_{x_1} . The method is also tested and proved to be robust with the distance uncertainties (10%) and the selection functions. The radial $\langle |v_R/v_{\text{tot}}| \rangle$ profile along the bar major axis after imitating the observation is shown by the blue dashed line in Fig. 8, in which the difference between the red and blue lines are negligible.

Applying this kinematic bar length measurement method to the Milky Way, we first rotate the stars in our sample by 25° to align the X -axis with the bar major axis. We fill the (X, Y) pixels that have no stars with $\langle |v_R/v_{\text{tot}}| \rangle$ equals 0. We plot the $\langle |v_R/v_{\text{tot}}| \rangle$ map of the rotated Milky Way on the top right panel of Fig. 8, and in the bottom, we plot the $\langle |v_R/v_{\text{tot}}| \rangle$ value as a function of radius along the bar major axis on the side that close to the Sun. The $\langle v_R/v_{\text{tot}} \rangle = 0.3$ happens at $R_b \approx 4.0$ kpc. Hence, we report $R_{b,\text{kin}} \approx 4.0$ kpc as a kinematic analogue of the dynamical length of the Milky Way bar. We denote this length by $R_{b,\text{kin}}$ to emphasise that this is

not a dynamical measurement but is instead a kinematic analogue. Note that this measurement of the bar length is independent of the Galactic potential and does not require the completeness of the sample as long as the sample gives enough coverage and sampling of the inner Galaxy.

3.5 Pattern speed estimates from the continuity equation

We can measure the pattern speed of the Galactic bar using the kinematics of LA-LPVs in our sample with the aid of the continuity equation. A critical issue when measuring the pattern speed of the Galactic bar using the continuity equation is the incompleteness of the observations as the stellar density is involved in the calculation. Bovy et al. (2019) find the pattern speed of the Galactic bar by applying the continuity equation to APOGEE stars with spectroscopic *AstroNN* distances. In Bovy et al. (2019), the selection function issue is omitted by postulating that the bar density is stratified on concentric ellipses. Dehnen et al. (2023) provides a method of estimating the pattern speed of the bar of a single simulation snapshot based on the continuity equation. They prove the method recovers the pattern speed of simulated galaxies, which has perfect completeness. The method in Dehnen et al. (2023) is also different to that in Bovy et al. (2019), in which Dehnen et al. (2023) compute the pattern speed by integrating the disc plane modulo a weighting function, while Bovy et al. (2019) bin stars into radial annulus. The weighting function proposed in Dehnen et al. (2023) behaves similarly to the selection function. Hence, choosing a proper weighting

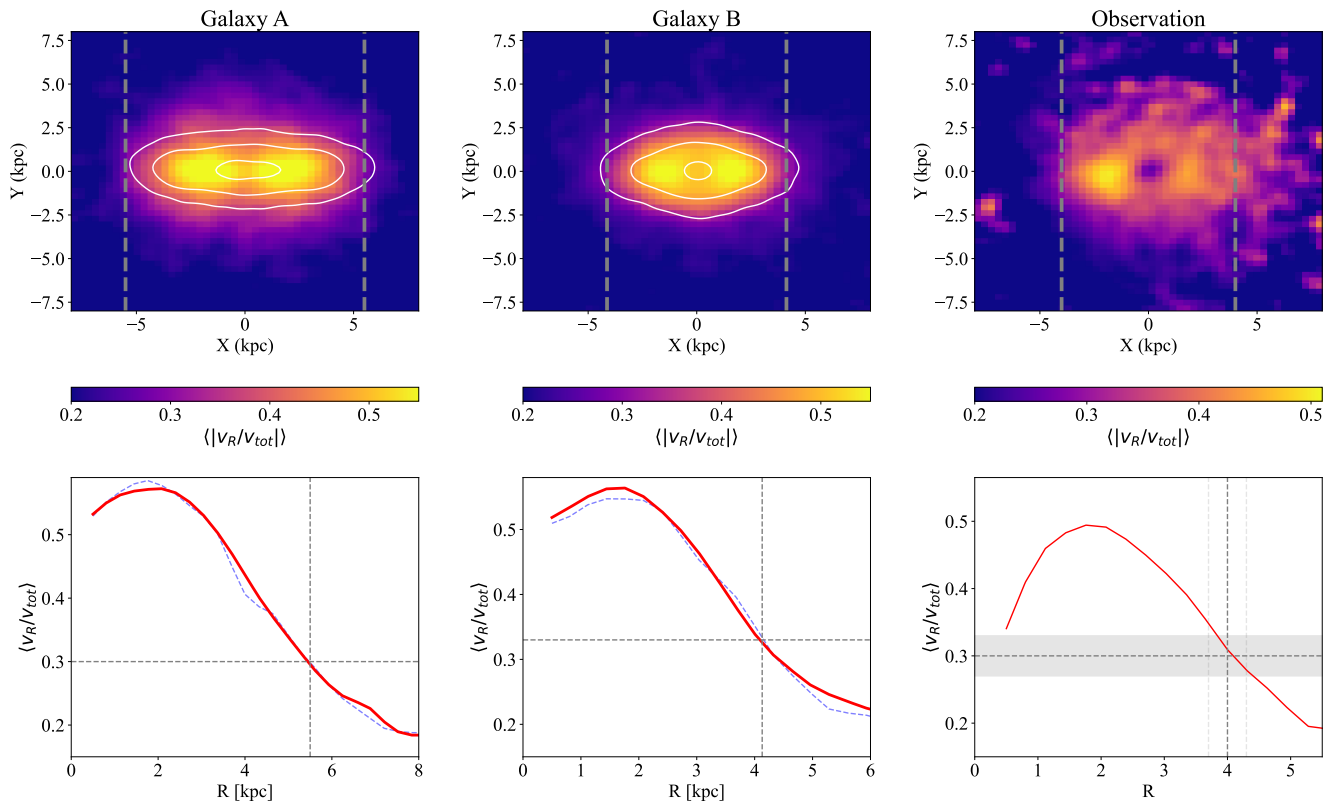


Figure 8. We compare the $\langle |v_R/v_{tot}| \rangle$ map and the distribution of the bar-supporting stars, and further, we compare the dynamical length of the bar to the extent of the signal in the $\langle |v_R/v_{tot}| \rangle$ map. The top panels show the $\langle |v_R/v_{tot}| \rangle$ map in Galaxy A, B and observed Milky Way, respectively. For the Milky Way map, we rotate the stars 25° clockwise to align the major axis of the bar with the X-axis. In the first two panels from the left, the white contours show the distribution of the bar stars selected from the orbital frequencies, which matches the signal in the $\langle |v_R/v_{tot}| \rangle$ map. The vertical grey dashed lines in the top left and middle panels label the spatial extent of the x_1 orbits in those two simulated galaxies, R_{x_1} . The grey dashed line in the right panel represents the radius that $\langle |v_R/v_{tot}| \rangle = 0.3$ along the major axis of the bar. In the bottom panels, we show the $\langle |v_R/v_{tot}| \rangle$ signal as a function radius along the major axis of the bar on the side that is close to the Sun. The red solid lines and blue dashed lines are the radial $\langle |v_R/v_{tot}| \rangle$ profile before and after applying the observational effects. The vertical dashed line is used to label the R_{x_1} , and we show that this generally corresponds to $\langle |v_R/v_{tot}| \rangle \approx 0.3$.

function also helps to mitigate the completeness problem. However, the weighting function in Dehnen et al. (2023) is only a function of the cylindrical radius (see Eq. 25 in Dehnen et al. 2023), so the selection function in the azimuthal direction still biases the pattern speed estimates.

As seen in the stellar density map shown in the top-left panel in Fig. 5, the density distribution tracks the shape of the bar and is roughly symmetric in the inner few kpc of the Galaxy. Compared to the APOGEE AstroNN sample in Bovy et al. (2019); Leung et al. (2023), we suffer less from the completeness issue in the $x-y$ plane at the inner Galaxy. This is because of the deep photometry from *Gaia* and the pure photometric selection of the LA-LPV candidates in our sample. The extinction does not seriously affect the construction of the catalogue, except for the missing ~ 150 pc above and below the plane. Hence, we attempt to directly apply the Fourier method in Dehnen et al. (2023) to our sample with a weighting function of $R_0 = 0.1$ kpc, $R_1 = 6$ kpc, and $R_m = 3$ kpc, where these parameters are defined by Eq. 25 in Dehnen et al. (2023). To understand the magnitude of bias due to the effects of heliocentric distance uncertainty and the selection function, we perform a test using the two N-body simulations presented above. We implement this method to the saved N-body snapshots with manually added uncertainties and selection functions for the two sets of N-body simulations (the same procedure as we used in the final column of

Fig. 7). Treating the pattern speed calculated from the finite difference method as the ground truth, we first apply the methods on the raw N-body snapshots (0 uncertainty, no incompleteness) to verify the method is implemented correctly. Then, we scatter the particles in the N-body simulation with 10% heliocentric distance uncertainty, and we further mimic the spatial selection function (SF) of our sample by matching the stars in the simulated galaxies to the observed spatial distribution. The method is tested on all three scenarios (1. no error, no SF; 2. 10% error, no SF; 3. 10% error, SF matched to observation) as validation. The result of this test is present in Fig. 9. Although both heliocentric distance uncertainty and incompleteness introduce bias in the pattern speed estimation, the test results generally agree with the ground truth pattern speed because neither effect is strong in our sample. Our test galaxies cover a range in pattern speeds and bar lengths and come from two independent N-body simulations. Hence, we argue that the Fourier method in Dehnen et al. (2023) can be directly applied to our sample and give a faithful estimation of the bar pattern speed.

The pattern speed estimated using this method on our sample is 34.1 ± 0.6 km s^{-1} kpc $^{-1}$. The uncertainty here is statistical and is propagated using the Monte Carlo method, in which we repeat 1000 random realisations of the measurements with the associated uncertainties. We calculate the pattern speed for each realisation and report the mean and standard deviation. With the N-body sim-

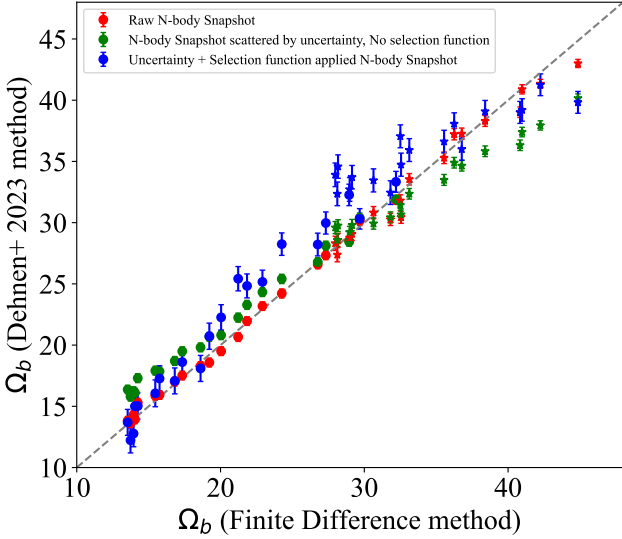


Figure 9. We show the validation results of applying the Fourier method in Dehnen et al. (2023) to the simulated galaxies with manually implemented selection functions and uncertainties. The circle dots are test results from N-body snapshots in Galaxy A, and the star dots are those in Galaxy B. The red dots are pattern speed estimates by applying the method directly to the raw N-body snapshots; the green dots are pattern speed estimates applying the methods on uncertainty-scattered snapshots; the blue dots are the method applied to the mock observed galaxies with both uncertainty and selection function. The grey dashed line shows the 1:1 line to the ground truth pattern speed.

ulation test, we can quantify the systematic uncertainty from the incompleteness and uncertainty effects on the continuity equation by calculating the standard deviation of the pattern speed residual. The systematic uncertainties brought by the selection effects are $\sim 2.3 \text{ km s}^{-1} \text{ kpc}^{-1}$.

As applying the continuity equation to a sample with imperfect uncertainty and completeness can introduce systematic biases, we suggest that the pattern speed reported above is an estimate instead of a robust measurement. The pattern speed could be consistent with other measurements when no assumption on the bar density distribution is made. To precisely get the pattern speed, more complicated methods should be employed, and we leave this for future works.

4 ORBITAL FAMILIES IN THE GALACTIC BAR

To analyse the dynamics of the Galactic bar, we need to assume a gravitational potential to integrate the orbits of stars. We employ the bar potential in Sormani et al. (2022), which is an analytic approximation of the M2M barred Milky Way model in Portail et al. (2017). Hence, all the results in this section are model-dependent. The chosen pattern speed for the potential is $34.1 \text{ km s}^{-1} \text{ kpc}^{-1}$, motivated by our measurements in Section 3.5, and we integrate stars for 1 Gyr. We use the same procedure in Section 3.4 to select bar stars and stars on x_1 orbits. Cutting on orbital frequency ($1.8 < \Omega_R/\Omega_X < 2.2$) and removing stars with apocentre greater than 6 kpc, we select a subsample of 1997 bar-supporting stars. Among these selected bar stars, $\sim 90\%$ have $\Omega_X/\Omega_Y \approx 1$, which are x_1 orbit candidates, while the remaining $\sim 10\%$ have Ω_X/Ω_Y between 0.6 and 0.8. Using the rigorous method of selecting x_1 orbits proposed

in Petersen et al. (2021), we further confirm 625 stars belong to x_1 orbital families. The spatial extension of the x_1 orbits is $R_{x_1} \sim 3.8 \text{ kpc}$, which is consistent with our kinematic analogue of the dynamical length measured in Section 3.4.

With a visual inspection of stars that failed the x_1 orbit selection, we find the majority still belong to the x_1 family tree. Most of them are bifurcated x_1 orbits with more loosely spaced apocentres; only a small fraction of the bar-supporting stars are not members of the x_1 orbital family. This confirms that the x_1 orbital family are still the main building block of the Galactic bar (Patsis & Athanassoula 2019; Petersen et al. 2021).

After selecting bar-supporting stars using orbital frequencies, we can access the orbital families using the ratio Ω_Z/Ω_X . Ω_Z/Ω_X is the ratio between the orbital frequencies in the vertical and bar major-axis direction, where stars with different ratios have different shapes in the edge-on projection of their orbits (Portail et al. 2015b). We plot the Ω_Z/Ω_X distribution of bar stars in the middle panel of Fig. 10. The blue line shows the orbital family distribution in our selected bar sample. The error is propagated using the Monte Carlo method, in which the pattern speed of the bar potential also participates in the random realisation. The effects of both the observational and pattern speed uncertainty are shown by the blue-shaded region in Fig 10 to represent the 1σ level scatter. We also perform the same analysis using different pattern speeds and find only a minor effect for the orbital families (as shown in the dashed red and black lines). An obvious trend in the spatial extension and orbital shape as a function of the Ω_Z/Ω_X is seen. We bin the bar-supporting stars in Ω_Z/Ω_X segments and calculate the mean apocentre radius, $\langle R_{\text{apo}} \rangle$, and $\langle X_{\text{max}}/Y_{\text{max}} \rangle$ for stars in the bin, in which X_{max} and Y_{max} are the maximum extension of an orbit along the bar major and minor axis. As shown in the top panel, orbits with greater Ω_Z/Ω_X extend farther from the Galactic centre and become more circular. Hence, with these results, we suggest no cuts on Ω_Z/Ω_X should be made when measuring the length of the bar because doing so could artificially shorten the measured bar length. We further illustrate this by plotting the spatial $X-Y$ distribution of the bar-supporting stars and colouring them by Ω_Z/Ω_X . The stars with higher Ω_Z/Ω_X reside in the outer region, which is similar to the simulated galaxies and M2M models in Portail et al. (2015b). The grey ellipse has a semi-major axis of 4 kpc, which we adopt from our $R_{b,\text{kine}}$ measurement in section 3.4. It shows consistency with selected bar-supporting stars.

Compared to the M2M model of the Milky Way in Portail et al. (2015b), we find a wider distribution in Ω_Z/Ω_X . Most stars in our sample have $\Omega_Z/\Omega_X < 3$ and there is a significant sub-population of stars with $\Omega_Z/\Omega_X \approx 2$. Orbits with $\Omega_Z/\Omega_X = 2$ are particularly interesting as they belong to $x_1 v_1$ family, sometimes called "banana" orbits due to their side-on projection (e.g., Skokos et al. 2002; Williams et al. 2016). These stars exhibit a 2 : 1 resonance in the vertical direction and used to be considered as the backbone of the X-shape in the boxy/peanut bulge due to the shape of their orbits. However, M2M models of the Milky Way bulge in Portail et al. (2015b) also revealed that "brezel" orbits can become a dominant contributor to the Galactic X-shape. The brezel orbits are stars in 5 : 3 vertical resonances ($\Omega_Z/\Omega_X \approx 5/3$). Unlike the orbital families distribution in Portail et al. (2015b), we still find banana orbits predominating with $\sim 15\%$ fractional contribution to the overall population. We present the spatial $X-Z$ distribution of stars belonging to banana orbits and brezel orbits in Fig. 11. Both orbital families trace the X-shaped bar; banana orbits contribute more stars, while the brezel orbits show a sharper X-shape. We also present the side-on projection of each orbital family in Appendix B to illustrate

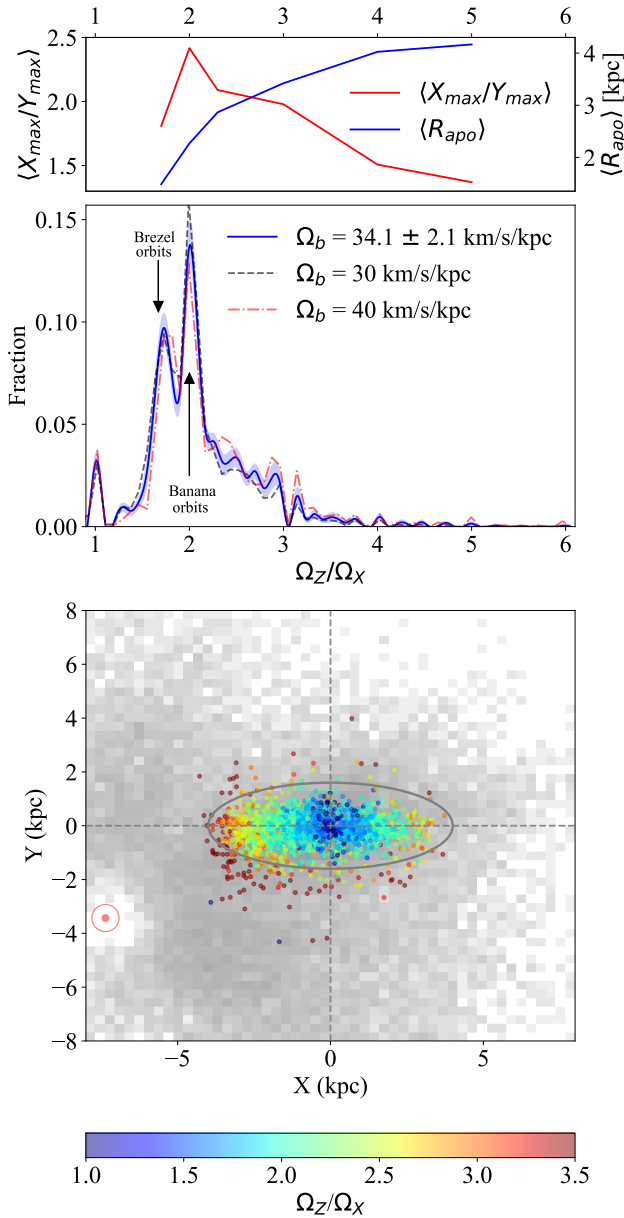


Figure 10. The orbital families in the bar-supporting orbits in terms of Ω_Z/Ω_X , which decides the vertical structures of orbits. The middle panel is the distribution of Ω_Z/Ω_X , in which the blue line and the blue-shaded region are the orbital family distribution and the associated 1σ uncertainty. The grey and red dashed lines are the Ω_Z/Ω_X when the pattern speed is 30 and 40 km/s/kpc. On the top panel, we show the mean apocentre, $\langle R_{apo} \rangle$, and mean $\langle X_{max}/Y_{max} \rangle$ for stars inside the corresponding Ω_Z/Ω_X segments in the blue and red lines, respectively. We illustrate the trends in $\langle R_{apo} \rangle$ as a function of Ω_Z/Ω_X in more detail on the bottom panel, in which the spatial distribution of bar-supporting stars are coloured by the Ω_Z/Ω_X value. The larger the Ω_Z/Ω_X , the greater the radial extension for the star's orbit. The background shows the 2D histogram of all stars in our sample rotated 25° to align the major axis of the bar to the X-axis.

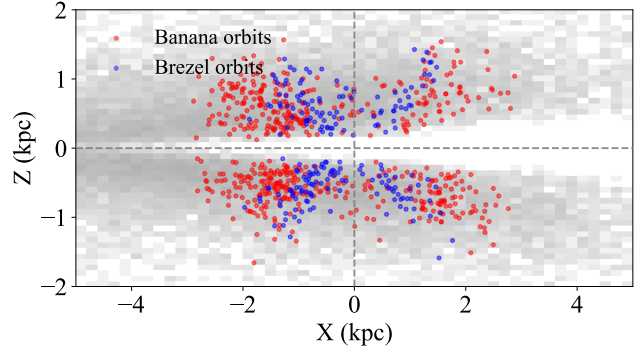


Figure 11. The spatial distribution of the stars that are assigned as banana orbits (red dots) and brezel orbits (blue dots). The background is the 2D histogram of all stars in our sample to show the selection function of our sample.

their contribution to bar density. Intriguingly, as revealed in Fig. 11, the X-shape structures contributed by different orbital families are different due to their spatial extension. We suggest that this signature provides scope for determining the more detailed structure in the X-shape, and also the main orbital family in the Galactic X-shaped structure.

We also test the impact of the selection function using the same spatial matching technique used previously on the Galaxy A. We test the selection function effect only on Galaxy A because it has similar orbital families to the Milky Way. We find that the selection function in our sample only gives a small adjustment from the raw orbital family distribution (see Fig. A1). The main selection effects we have are 1) stars in ~ 150 pc above and below the plane are missing 2) the outskirts of the bar on the far side of the disc are less complete and suffer greater distance uncertainty. After applying the selection function, the relative fraction of stars with banana orbits is slightly enhanced as they spend more time outside the Galactic plane. Stars with $\Omega_Z/\Omega_X \geq 2.5$ are slightly depleted because we miss some of these stars on the far side of the Galaxy. A more detailed discussion of the selection function impact is in Appendix A. However, due to the satisfactory completeness of this sample in the inner Galaxy, both effects are mild. Therefore, we conclude that the banana orbits, x_1v_1 family, contribute most to the Galactic X-shape bar, but contributions from higher-order resonances are also non-negligible.

5 DISCUSSION AND COMPARISON

Hilmi et al. (2020) show that the bar-spiral interaction could bias the instantaneous measurements of the Galactic bar parameters. The bar length can be overestimated due to the bar-spiral coupling and constructive interference in the overlapping region. They also argued that the pattern speed measurement using the modified Tremaine-Weinberg method in Sanders et al. (2019b) can lead to a fluctuation of 10 – 20% around the mean when the bar is connected to a spiral arm. The Scutum–Centaurus arm is likely connected to the spiral arm at the present day (Rezaei Kh. et al. 2018). We devote this section to discussing the implications of the bar-spiral interaction in our results and comparing our measurements with those of previous studies.

5.1 Bar length

We do not measure the bar length using any density-based method due to the bar-spiral interaction. Instead, we rely on a kinematic measurement of the bar length as an analogue to the dynamical length. The dynamical length should be less affected by the Scutum–Centaurus arm as we trace the signature of bar-supporting orbits instead of the density of stars. In our case, we use the mean radial fraction of the total velocity map, $\langle |v_R/v_{\text{tot}}| \rangle$, which has a high value when the region is dominated by bar-supporting orbits as demonstrated in Section 3.4. Checking the N-body snapshots, which also have spiral arms connected to the bar, we also find a small signal (under the $\langle |v_R/v_{\text{tot}}| \rangle = 0.3$ threshold adopted above) in the $\langle |v_R/v_{\text{tot}}| \rangle$ map in the spiral region, but it is insignificant compared to the signal from the bar stars. This indicates that the dynamics of stars in the spiral arm differ from that of disc stars but contribute mildly compared to the bar. The comparison we ran with length estimated by the x_1 orbits, R_{x_1} , serves the same purpose, which shows that the $\langle |v_R/v_{\text{tot}}| \rangle$ map can trace the length of the bar without much effect from the bar-spiral interaction. This kinematic analogue of dynamical length is also a model-independent measurement of the bar length without requiring a gravitational potential. If we assume knowledge of the potential in the inner Galaxy as done in the dynamical analysis in Section 4, we can also classify the stars with x_1 orbits from our sample and determine the bar length using the x_1 orbits. Using the potential from Sormani et al. (2022), R_{x_1} for the Milky Way is 3.8 kpc, which is in agreement with its kinematic analogue $R_{b,\text{kin}} = 4.0$ kpc. However, we do not further discuss the R_{x_1} measurement of the Milky Way as it is model-dependent.

We argued in Section 3.4 that the $\langle |v_R/v_{\text{tot}}| \rangle$ map traces the distribution of bar-supporting stars. Therefore, galactic bars comprised of different bar-supporting families could have different $\langle |v_R/v_{\text{tot}}| \rangle$ maps. This is demonstrated by the top panels in Fig. 8, in which the $\langle |v_R/v_{\text{tot}}| \rangle$ maps have different shapes in Galaxy A and B because the orbital families are different. Galaxy A has orbital families as shown in Fig. A similar to the observation of the Milky Way bar; while Galaxy B has orbital families similar to the M2M model in Portail et al. (2015b), in which over 95% of stars have $\Omega_Z/\Omega_X \lesssim 2$. However, despite the difference in the orbital family distribution, the dynamical length corresponds to $\langle |v_R/v_{\text{tot}}| \rangle \approx 0.3$ for both galaxies. Therefore, testing on both Galaxy A and B reinforces the robustness of the method.

Measuring the dynamical length using the $\langle |v_R/v_{\text{tot}}| \rangle$ map is similar to the method proposed by Petersen et al. (2024), which uses the v_{\perp} map. However, as we argued in Section 3.4, our method is more suitable when the full 6D phase space of individual stars is measured, while the method in Petersen et al. (2024) is better when the kinematic measurement is limited but has high signal-to-noise, which is better to implement on extragalactic observations.

Now, we compare the kinematic analogue of dynamical length in this work, $R_{b,\text{kin}} = 4.0$ kpc, to other previous dynamical length measurements of the Galactic bar. Lucey et al. (2023) measures the "dynamical" length of the bar, defined by the apocentric radius of bar-supporting stars (not x_1 orbits), in various simulated galaxies. Combining the APOGEE and Gaia data, they integrate the observed Milky Way stars using the potential in the simulated galaxies with the same pattern speed of $\Omega_b = 41 \text{ km s}^{-1} \text{ kpc}^{-1}$ and measure the same dynamical length for the Milky Way bar, and they find the simulated galaxy with the closest dynamical length as the best Milky Way surrogate. Lucey et al. (2023) reports both a "dynamical" length $R_{\text{freq}} = 3.2$ kpc and $R_{x_1} = 3.5$ kpc of that Milky Way surrogate galaxy as the bar length of the Milky Way (we use the same notation

as Lucey et al. (2023) for clarity). The R_{x_1} measurement is still in broad agreement with our results, but the R_{freq} length is much shorter than our measurement. This could be because the pattern speed used in Lucey et al. (2023) is faster than our measurement and also greater than the most recent measurement using resonances in the Galactic halo (Dillamore et al. 2024), which would cause the bar length to be underestimated. Hence, the best-matched galaxies may also change if a different pattern speed is chosen. Also, in Lucey et al. (2023), a cut on $\Omega_Z/\Omega_X \lesssim 3.3$ is applied when selecting bar-supporting stars. As we illustrate in Fig. 10 (also see Portail et al. 2015b), this effectively is a cut on the apocentre distribution of bar-supporting stars, causing the bar length to be underestimated.

Vislosky et al. (2024) compared the radial velocity field, \bar{V}_R map, in Gaia DR3 with the cosmological and N-body simulations while taking the bar-spiral interaction into account. They find a consistent radial velocity field of galaxies that either have a short bar with a strong spiral arm or a long bar with a weak spiral feature. Our $R_{b,\text{kin}}$ measurement is more consistent with their short bar model, which has $R_b \sim 3.6$ kpc. Overall, the dynamical length measured in this work agrees with previous studies and is unique as a model-independent measurement.

5.2 Pattern speed

The pattern speed is estimated using the method developed in Dehnen et al. (2023), which builds on the continuity equation and is a 2D extension of the Tremaine-Weinberg (TW) method (Tremaine & Weinberg 1984). Hilmi et al. (2020) showed that the pattern speed estimation using the modified TW method in Sanders et al. (2019b) can lead to fluctuation up to 20%. However, in Dehnen et al. (2023), they test the method with two sets of N-body simulations, and one of them (the "fiducial model" therein) has transient spiral arm features. The method successfully recovers the true pattern speed. This is the same as in our work. Many snapshots in our N-body simulation also show spiral features connected to the bar, and the pattern speeds recovered using the method do not deviate significantly from the true pattern speed calculated using the finite difference method. Hence, we argue the bar-spiral interaction does not have a strong effect on our measurement. Also, as the bar-spiral interaction scenario happens in our tested galaxies, any fluctuation caused by the method is included in the reported systematic uncertainty.

The pattern speed measured is $\Omega_b = 34.1 \pm 2.4 \text{ km s}^{-1} \text{ kpc}^{-1}$, in which the uncertainty includes both random and systematic error. This value is consistent with many recent measurements using a variety of different methods, including M2M and resonances features in the solar neighbourhood (Clarke & Gerhard 2022; Binney 2020; Chiba & Schönrich 2021; Kawata et al. 2021; Dillamore et al. 2023, 2024).

Resonance features in the solar neighbourhood provide important constraints for pattern speed measurements. Binney (2020) studied the kinematics in the solar neighbourhood and stars trapped by the bar resonance orbits and concluded a pattern speed of $\Omega_b = 35.2 \pm 1.0 \text{ km s}^{-1} \text{ kpc}^{-1}$. Chiba & Schönrich (2021) used the metallicity gradient of resonance stars caused by the slowing-down bar and show that the pattern speed is $\Omega_b = 35.5 \pm 0.8 \text{ km s}^{-1} \text{ kpc}^{-1}$. Kawata et al. (2021) find the pattern speed of 34 or 42 $\text{km s}^{-1} \text{ kpc}^{-1}$ can both well-explain the local moving groups, in which the lower value is consistent with our measurements. Halo substructures also become tracers of bar pattern speed. Dillamore et al. (2023) first show that the bar resonances stars in the halo form constant energy ridges in the $E - L_z$ space. Combining with Gaia data, they find the ridges are consistent with the pattern speed of

35 – 40 km s⁻¹ kpc⁻¹. Then, [Dillamore et al. \(2024\)](#) extended the theory to $r - v_r$ space and explained the phase space chevron in [Belokurov et al. \(2023\)](#) with bar resonances with a pattern speed of 35 km s⁻¹ kpc⁻¹. Pattern speed measurements are also taken by directly observing the Galactic bar. [Clarke et al. \(2019\)](#) compared data from the Variables in the Via Lactea (VVV) survey and *Gaia* DR2 with M2M models in [Portail et al. \(2017\)](#), qualitatively and found a pattern speed measurement of 37.5 km s⁻¹ kpc⁻¹. Later, with quantitative analysis, the pattern speed measurement was lowered to 33.3 ± 1.8 km s⁻¹ kpc⁻¹ ([Clarke & Gerhard 2022](#)). All of these pattern speeds yielded by studying both the solar neighbourhood and the bar directly agree with the value measured using the continuity equation in this work.

However, earlier implementations of the continuity equation reported higher pattern speeds than ~ 34 km s⁻¹ kpc⁻¹ ([Sanders et al. 2019b](#); [Bovy et al. 2019](#); [Leung et al. 2023](#)). [Sanders et al. \(2019b\)](#) also showed that the pattern speed measurements become 31 km s⁻¹ kpc⁻¹ when considering data on both sides of the bar, which suggested a 5 – 10 km s⁻¹ kpc⁻¹ systematic error on the measurement. Also, the method used in [Sanders et al. \(2019b\)](#) is sensitive to the foreground and background perturbation because the continuity equation is integrated along the line-of-sight, which could be responsible for the fluctuation in the pattern speed measurements seen from the simulations in [Hilmi et al. \(2020\)](#). The spiral features are better handled in [Dehnen et al. \(2023\)](#) because of the weighting function involved in the pattern speed calculation. [Bovy et al. \(2019\)](#) used *Gaia* and APOGEE *AstroNN* distances to analyse the chemo-dynamic property of the Galactic bar. Applying the continuity equation with a pre-assumed exponential ellipsoidal density profile to the data produces a pattern speed of 41 ± 3 km s⁻¹ kpc⁻¹. The value was later updated to 40.1 ± 1.8 km s⁻¹ kpc⁻¹ in [Leung et al. \(2023\)](#) with an updated dataset. One possible explanation for the discrepancy could be the assumed density distribution. The suitability of the assumed ellipsoidal density distribution needs to be further tested. The difference could also be attributed to the incompleteness of observation due to the spectroscopic nature of the dataset. It is also shown in [Bovy et al. \(2019\)](#) that the pattern speed measurements varied 3 – 5 km s⁻¹ kpc⁻¹ when changing the Sun's distance of the Galactic centre, the radial density gradient and the flattening of the ellipsoid.

5.3 Influence of a larger distance uncertainty

As shown in Section 2, the median fractional distance uncertainty is $\sim 10\%$, which is contributed by the intrinsic scatter of OSARG's PLR from [Soszyński et al. \(2007\)](#), and the period uncertainty reported by the *Gaia* LPV catalogue ([Lebzelter et al. 2023](#)). However, the intrinsic scatter of the PLR is still under debate. A different calibration method applied on the same dataset (OGLEIII LMC, [Soszyński et al. 2007, 2009](#)) yields different distance uncertainty ([Soszyński et al. 2007](#); [Rau et al. 2019](#); [Hey et al. 2023](#); Zhang et al. in prep.). The parameterised PLR we adopted from [Soszyński et al. \(2007\)](#) showed intrinsic scatter that leads to less than 10% distance uncertainty, which was calibrated using linear regression. [Rau et al. \(2019\)](#) trained a machine learning model using the Random Forest ([Breiman 2001](#)) and reported a similar scatter. [Hey et al. \(2023\)](#) calibrated the LA-LPV distances using kernel density estimation, but the distance uncertainty reported is $\sim 15\%$. Zhang et al. (in prep.) use a similar method as that in [Rau et al. \(2019\)](#) and show that the distance uncertainty is $\sim 10\%$ by comparing the calibrated luminosity distance to the globular cluster members with known distances. The distance uncertainties of the LA-LPV candidates in

our sample are on the lower side of these measurements because we used the PLR from [Soszyński et al. \(2007\)](#). The actual uncertainty could tend more towards 15% as shown in [Hey et al. \(2023\)](#).

To verify the validity of the analysis and results, we perform similar tests to the bar length and the pattern speed as above but with 15% distance uncertainty instead of 10%. The radial $\langle |v_R/v_{\text{tot}}| \rangle$ profile along the bar major axis varies little when the distance uncertainty increases. The pattern speed estimation becomes more biased with larger distance uncertainty, and the estimated pattern speed is shown to be underestimated when the pattern speed is large, but a 1:1 consistency between the true and recovered pattern speed is still seen in most of the N-body simulation snapshots. Therefore, we argued that the results we obtained above are still valid even if the distance uncertainty is underestimated. The details are shown on Fig. C1 and C2 in Appendix C.

6 CONCLUSIONS

We use LA-LPVs (mainly OSARGs) as tracers to investigate the kinematic and dynamic structures of the inner Milky Way. We use the LPV catalogue of *Gaia* DR3 to select low-amplitude LPVs as LA-LPV candidates. We assign the distance moduli of OSARGs using their period-luminosity relations calibrated in the Milky Way. We validate the assigned distances by comparing common stars in various samples, including geometric distances with good fractional parallax uncertainty, spectroscopic-based StarHorse distances, and globular cluster members. We demonstrate a good performance of the assigned distances with the median uncertainty of $\sim 10\%$. We also compare the radial velocity uncertainties of the selected OSARGs to a randomly selected *Gaia* DR3 sample and show that the radial velocity measurements of these LA-LPVs are reliable. We show the face-on view of our sample, which covers a large region in the Galactic disc and has considerable coverage on the far side of the Galaxy. Our sample covers heliocentric distances between $\sim 1 - 18$ kpc and Galactocentric radii between $0 - 15$ kpc. Due to the photometric nature of the sample selection and the full-sky coverage of the *Gaia* mission, there is only a weak spatial selection function.

Our main results are:

(i) We map the kinematic field of the inner Galaxy in terms of the mean radial, azimuthal and vertical velocity ($\overline{V_R}, \overline{V_\phi}, \overline{V_z}$), and radial velocity dispersion (σ_R^*) in Fig. 5. The quadrupole, or butterfly pattern, in the $\overline{V_R}$ field is conspicuous confirming the existence of the bar in our sample. No systematic pattern is observed in the $\overline{V_z}$ map.

(ii) We kinematically detect the Galactic bar using the mean radial fraction of the total velocity map, $\langle |v_R/v_{\text{tot}}| \rangle$. We expect a high value of $\langle |v_R/v_{\text{tot}}| \rangle$ in the bar region due to the elongated orbits of bar-supporting stars. We observe an obvious signal in the $\langle |v_R/v_{\text{tot}}| \rangle$ map in our sample corresponding to the shape of the bar and we verify the usefulness of this map using N-body simulations.

(iii) Imitating the observational uncertainty and selection function in a simulated galaxy, we find excellent consistency with our observed kinematic maps. This validates the quality of our sample. We find the heliocentric distance uncertainty biases the bar signature in the stellar density map and $\overline{V_R}$ map to align with the Sun-GC line, as expected ([Hey et al. 2023](#); [Vislosky et al. 2024](#)). However, we also see that the orientation of the bar revealed by the $\langle |v_R/v_{\text{tot}}| \rangle$ map is more robust against the heliocentric distance uncertainty. Hence, we use the signal in $\langle |v_R/v_{\text{tot}}| \rangle$ to give a crude estimate of

the bar angle of 25° , which is consistent with other studies (Wegg & Gerhard 2013; Simion et al. 2017; Clarke et al. 2019; Bovy et al. 2019).

(iv) We propose a model-independent, purely kinematic method of measuring the dynamical length of the bar using the $\langle |v_R/v_{\text{tot}}| \rangle$ map. We demonstrate that this map traces the orbital features of the bar-supporting stars by confirming a consistent spatial match between the bar-supporting stars and the $\langle |v_R/v_{\text{tot}}| \rangle$ map in those galaxies. More quantitatively, we find the bar length defined by x_1 orbits, R_{x_1} , corresponds to $\langle v_R/v_{\text{tot}} \rangle|_{R_b} \approx 0.3$. Using this feature, we measure the kinematic analogue of the dynamical length of the bar as $R_{b,\text{kine}} \sim 4.0$ kpc.

(v) We measure the bar pattern speed using the method developed in Dehnen et al. (2023), which was designed to extract the pattern speed from single simulation snapshots using the continuity equation. We demonstrate that the method also has good applicability to our data by applying the method on snapshots from N-body simulations after applying observational effects; only small systematic biases and uncertainties are induced by the measurement errors and the selection function. The pattern speed obtained is $34.1 \pm 2.4 \text{ km s}^{-1} \text{ kpc}^{-1}$, which is consistent with the values from many studies of the resonance features in the solar neighbourhood (Binney 2020; Kawata et al. 2021; Chiba & Schönrich 2021; Dillamore et al. 2023, 2024) and direct observation in the bar (Clarke & Gerhard 2022).

(vi) We use the potential in Sormani et al. (2022) to integrate the orbits and compute the orbital frequencies, Ω_i . Selecting bar stars using their orbital frequencies ratio, we find $\sim 2,000$ bar-supporting stars in our sample. We study the vertical structure of orbits using the Ω_Z/Ω_X ratio finding stars with greater Ω_Z/Ω_X reside farther away from the centre in agreement with Portail et al. (2015b).

(vii) We securely identify ~ 600 x_1 -orbital stars out of 2,000 bar stars. Using visual inspection for the rest of the stars, we find the majority also belong to the x_1 family tree. Moreover, $\sim 90\%$ of bar stars have $\Omega_X/\Omega_Y \sim 1$, hinting that they are x_1 orbit candidates. Hence, we conclude that the x_1 family constitutes the main building block of the Galactic bar.

(viii) Unlike the M2M model of the Galactic bulge built in Portail et al. (2015b), we find an abundance of x_1v_1 banana orbits amongst our selected bar stars, suggesting they are the main constituents of the Galactic X-shape. This is in contrast to the predominance of the "brezel" orbits proposed by Portail et al. (2015b). Plotting the spatial distribution of the banana and brezel orbits on the $X-Z$ plane, we see clear X-shaped structures; while banana orbits contribute more stars, brezel orbits give a sharper X-shape.

For future work, we plan to include the metallicity measurements of these LA-LPV using *Gaia* XP spectrum to expand the information to 7D or 8D. Then, a full chemo-dynamical analysis can be performed on this sample. A preliminary result suggests our LA-LPV sample covers a large range of metallicity from -1.5 to 0.5 dex.

DATA AVAILABILITY

Gaia data used in this work is publicly available. The sample constructed in this work will be publicly available after the paper is accepted. Before that, all data underlying this paper will be shared on reasonable request to the corresponding author.

ACKNOWLEDGEMENTS

We thank Adam Dillamore and Elliot Davies for their inspirational discussions and for their help in setting up the N-body simulations. We thank Eugene Vasiliev for helpful comments on the draft of the paper.

HZ thanks the Science and Technology Facilities Council (STFC) for a PhD studentship. VB acknowledges support from the Leverhulme Research Project Grant RPG-2021-205: "The Faint Universe Made Visible with Machine Learning". SK thanks the Marshall Scholarship for her PhD funding. JLS acknowledges support from the Royal Society (URFR1\191555).

This work has made use of data from the European Space Agency (ESA) mission *Gaia* (<https://www.cosmos.esa.int/gaia>), processed by the *Gaia* Data Processing and Analysis Consortium (DPAC, <https://www.cosmos.esa.int/web/gaia/dpac/consortium>). Funding for the DPAC has been provided by national institutions, in particular the institutions participating in the *Gaia* Multilateral Agreement.

REFERENCES

- Ardern-Arentsen A., et al., 2024, *MNRAS*, 530, 3391
 Athanassoula E., Misiriotis A., 2002, *MNRAS*, 330, 35
 Bailer-Jones C. A. L., Rybizki J., Fousneau M., Demleitner M., Andrae R., 2021, *AJ*, 161, 147
 Belokurov V., Vasiliev E., Deason A. J., Koposov S. E., Fattahi A., Dillamore A. M., Davies E. Y., Grand R. J. J., 2023, *MNRAS*, 518, 6200
 Binney J., 2010, *MNRAS*, 401, 2318
 Binney J., 2020, *MNRAS*, 495, 895
 Binney J., Gerhard O. E., Stark A. A., Bally J., Uchida K. I., 1991, *MNRAS*, 252, 210
 Bland-Hawthorn J., Gerhard O., 2016, *ARA&A*, 54, 529
 Blitz L., Spergel D. N., 1991, *ApJ*, 379, 631
 Bovy J., Leung H. W., Hunt J. A. S., Mackereth J. T., García-Hernández D. A., Roman-Lopes A., 2019, *MNRAS*, 490, 4740
 Breiman L., 2001, *Mach. Learn.*, 45, 5
 Cardelli J. A., Clayton G. C., Mathis J. S., 1989, *ApJ*, 345, 245
 Catchpole R. M., Whitelock P. A., Feast M. W., Hughes S. M. G., Irwin M., Alard C., 2016, *MNRAS*, 455, 2216
 Chiba R., Schönrich R., 2021, *MNRAS*, 505, 2412
 Clarke J. P., Gerhard O., 2022, *MNRAS*, 512, 2171
 Clarke J. P., Wegg C., Gerhard O., Smith L. C., Lucas P. W., Wylie S. M., 2019, *MNRAS*, 489, 3519
 Davies E. Y., Dillamore A. M., Vasiliev E., Belokurov V., 2023, *MNRAS*, 521, L24
 Dehnen W., 2000, *ApJ*, 536, L39
 Dehnen W., Semečuk M., Schönrich R., 2023, *MNRAS*, 518, 2712
 Dillamore A. M., Belokurov V., Evans N. W., Davies E. Y., 2023, *MNRAS*, 524, 3596
 Dillamore A. M., Belokurov V., Evans N. W., 2024, *arXiv e-prints*, p. arXiv:2402.14907
 Englmaier P., Gerhard O., 1999, *MNRAS*, 304, 512
 Eyer L., et al., 2023, *A&A*, 674, A13
 Feast M. W., Whitelock P. A., 2000, *MNRAS*, 317, 460
 Fragkoudi F., et al., 2020, *MNRAS*, 494, 5936
 Fujii M. S., Bédorf J., Baba J., Portegies Zwart S., 2018, *MNRAS*, 477, 1451
 Fux R., 1999, *A&A*, 345, 787
 Gaia Collaboration et al., 2023a, *A&A*, 674, A1
 Gaia Collaboration et al., 2023b, *A&A*, 674, A37
 Grady J., Belokurov V., Evans N. W., 2019, *MNRAS*, 483, 3022
 Grady J., Belokurov V., Evans N. W., 2020, *MNRAS*, 492, 3128
 Hey D. R., et al., 2023, *AJ*, 166, 249
 Hilmi T., et al., 2020, *MNRAS*, 497, 933

- Iwanek P., et al., 2023, *ApJS*, 264, 20
- Kawata D., Baba J., Hunt J. A. S., Schönrich R., Ciucă I., Friske J., Seabroke G., Cropper M., 2021, *MNRAS*, 508, 728
- Kochanek C. S., et al., 2017, *PASP*, 129, 104502
- Lebzelter T., et al., 2023, *A&A*, 674, A15
- Lemasle B., et al., 2022, *A&A*, 668, A40
- Leung H. W., Bovy J., Mackereth J. T., Hunt J. A. S., Lane R. R., Wilson J. C., 2023, *MNRAS*, 519, 948
- Li Z., Shen J., Gerhard O., Clarke J. P., 2022, *ApJ*, 925, 71
- Liao X., Li Z.-Y., Simion I., Shen J., Grand R., Fragkoudi F., Marinacci F., 2024, *ApJ*, 967, 5
- Lloyd S., 1982, *IEEE Transactions on Information Theory*, 28, 129
- Lucey M., Pearson S., Hunt J. A. S., Hawkins K., Ness M., Petersen M. S., Price-Whelan A. M., Weinberg M. D., 2023, *MNRAS*, 520, 4779
- Matsunaga N., Kawadu T., Nishiyama S., Nagayama T., Hatano H., Tamura M., Glass I. S., Nagata T., 2009, *MNRAS*, 399, 1709
- Matsunaga N., et al., 2023, *ApJ*, 954, 198
- McMillan P. J., 2017, *MNRAS*, 465, 76
- McWilliam A., Zoccali M., 2010, *ApJ*, 724, 1491
- Mowlavi N., et al., 2018, *A&A*, 618, A58
- Nakada Y., Onaka T., Yamamura I., Deguchi S., Hashimoto O., Izumiura H., Sekiguchi K., 1991, *Nature*, 353, 140
- Nataf D. M., Udalski A., Gould A., Fouqué P., Stanek K. Z., 2010, *ApJ*, 721, L28
- Nishiyama S., Tamura M., Hatano H., Kato D., Tanabé T., Sugitani K., Nagata T., 2009, *ApJ*, 696, 1407
- Paterson D., Coleman B., Gordon C., 2020, *MNRAS*, 499, 1937
- Patsis P. A., Athanassoula E., 2019, *MNRAS*, 490, 2740
- Peters W. L. I., 1975, *ApJ*, 195, 617
- Petersen M. S., Weinberg M. D., Katz N., 2021, *MNRAS*, 500, 838
- Petersen M. S., Weinberg M. D., Katz N., 2024, *MNRAS*, 531, 1163
- Pietrzyński G., et al., 2019, *Nature*, 567, 200
- Portail M., Wegg C., Gerhard O., Martinez-Valpuesta I., 2015a, *MNRAS*, 448, 713
- Portail M., Wegg C., Gerhard O., 2015b, *MNRAS*, 450, L66
- Portail M., Gerhard O., Wegg C., Ness M., 2017, *MNRAS*, 465, 1621
- Posti L., Binney J., Nipoti C., Ciotti L., 2015, *MNRAS*, 447, 3060
- Prudil Z., et al., 2022, *A&A*, 664, A148
- Queiroz A. B. A., et al., 2020, *A&A*, 638, A76
- Queiroz A. B. A., et al., 2021, *A&A*, 656, A156
- Rau M. M., Koposov S. E., Trac H., Mandelbaum R., 2019, *MNRAS*, 484, 409
- Rezaei Kh. S., Bailer-Jones C. A. L., Hogg D. W., Schultheis M., 2018, *A&A*, 618, A168
- Rosas-Guevara Y., et al., 2022, *MNRAS*, 512, 5339
- Sanders J. L., 2023, *MNRAS*, 523, 2369
- Sanders J. L., Matsunaga N., 2023, *MNRAS*, 521, 2745
- Sanders J. L., Smith L., Evans N. W., Lucas P., 2019a, *MNRAS*, 487, 5188
- Sanders J. L., Smith L., Evans N. W., 2019b, *MNRAS*, 488, 4552
- Sanders J. L., Matsunaga N., Kawata D., Smith L. C., Minniti D., Lucas P. W., 2022, *MNRAS*, 517, 257
- Sanders J. L., Kawata D., Matsunaga N., Sormani M. C., Smith L. C., Minniti D., Gerhard O., 2024, *MNRAS*, 530, 2972
- Schönrich R., Binney J., Dehnen W., 2010, *MNRAS*, 403, 1829
- Semczuk M., Dehnen W., Schönrich R., Athanassoula E., 2022, *MNRAS*, 509, 4532
- Simion I. T., Belokurov V., Irwin M., Koposov S. E., Gonzalez-Fernandez C., Robin A. C., Shen J., Li Z. Y., 2017, *MNRAS*, 471, 4323
- Skokos C., Patsis P. A., Athanassoula E., 2002, *MNRAS*, 333, 847
- Skrutskie M. F., et al., 2006, *AJ*, 131, 1163
- Sormani M. C., Binney J., Magorrian J., 2015, *MNRAS*, 454, 1818
- Sormani M. C., Gerhard O., Portail M., Vasiliev E., Clarke J., 2022, *MNRAS*, 514, L1
- Soszyński I., Udalski A., Kubiak M., Szymański M., Pietrzyński G., Żebruń K., Szezwycyk O., Wyrzykowski Ł., 2004, *Acta Astron.*, 54, 129
- Soszyński I., et al., 2007, *Acta Astron.*, 57, 201
- Soszyński I., et al., 2009, *Acta Astron.*, 59, 239
- Soszyński I., et al., 2013, *Acta Astron.*, 63, 21
- Stanek K. Z., Udalski A., Szymański M., Kałużny J., Kubiak Z. M., Mateo M., Krzemiński W., 1997, *ApJ*, 477, 163
- Tabur V., Bedding T. R., Kiss L. L., Giles T., Derekas A., Moon T. T., 2010, *MNRAS*, 409, 777
- Tepper-García T., et al., 2021, *arXiv e-prints*, p. arXiv:2111.05466
- Trabucchi M., Mowlavi N., 2022, *A&A*, 658, L1
- Trabucchi M., Mowlavi N., Lebzelter T., 2021, *A&A*, 656, A66
- Tremaine S., Weinberg M. D., 1984, *ApJ*, 282, L5
- Udalski A., Szymanski M., Kaluzny J., Kubiak M., Mateo M., 1992, *Acta Astron.*, 42, 253
- VanderPlas J. T., 2018, *ApJS*, 236, 16
- Vasiliev E., 2019, *MNRAS*, 482, 1525
- Vasiliev E., Baumgardt H., 2021, *MNRAS*, 505, 5978
- Vislosky E., et al., 2024, *MNRAS*, 528, 3576
- Wegg C., Gerhard O., 2013, *MNRAS*, 435, 1874
- Wegg C., Gerhard O., Portail M., 2015, *MNRAS*, 450, 4050
- Williams A. A., Evans N. W., 2015, *MNRAS*, 448, 1360
- Williams A. A., et al., 2016, *ApJ*, 824, L29
- Wood P. R., 2000, *Publ. Astron. Soc. Australia*, 17, 18
- Wray J. J., Eyer L., Paczyński B., 2004, *MNRAS*, 349, 1059
- Zhang H., Sanders J. L., 2023, *MNRAS*, 521, 1462

APPENDIX A: EFFECT OF SELECTION FUNCTION ON THE ORBITAL FAMILY DISTRIBUTION

Although we show that the selection function (SF) affects our kinematic results only weakly, the significance of the SF effects on the dynamics is also worth testing. To achieve this, we employ the N-body simulated Galaxy A because it has a similar Ω_Z/Ω_X distribution to the observations. We use the same techniques of applying the selection function to the simulation by matching the simulated particles to observed stars in the spatial distribution. Matching every observed star to a simulated star that is closest to it in $x - y - z$ space, we drop all simulated particles that failed to become the closest match to observation or for which the closest matched distance is greater than 0.5 kpc. After this procedure, the number of simulated particles is roughly the same as the observed number of stars, and the spatial distribution is almost identical. Selecting bar-supporting stars using the same method in Section 4, the orbital distribution is shown in Fig. A1, in which the red line shows the raw distribution before applying SF, and the black is the distribution after applying SF to Galaxy A.

As we mentioned in Section 2, the main selection effects in our sample are that 1) the inner ~ 150 pc of the Galaxy is missing due to dust extinction and 2) the far side of the disc is not mapped as completely as the near side. This introduces two effects that could potentially affect our conclusion. The banana orbits at $\Omega_Z/\Omega_X = 2$ are slightly enhanced since they stay out of the galactic plane more than the other families. The orbits with $\Omega_Z/\Omega_X \gtrsim 2.5$ are slightly depleted because they tend to extend farther away from the galactic centre, and therefore, they are mainly observed on the near-side of the disc, while the families with smaller Ω_Z/Ω_X are observed on both sides. However, as evident in Fig. A1, both effects are small. We check the SF effects on the Ω_X/Ω_Y distribution and find the changes are also insignificant. Combining with the minor effects from the uncertainty as we see in Fig. 10, we therefore argue that the orbital family distribution we find in Section 4 is close to the real distribution in the Milky Way bar.

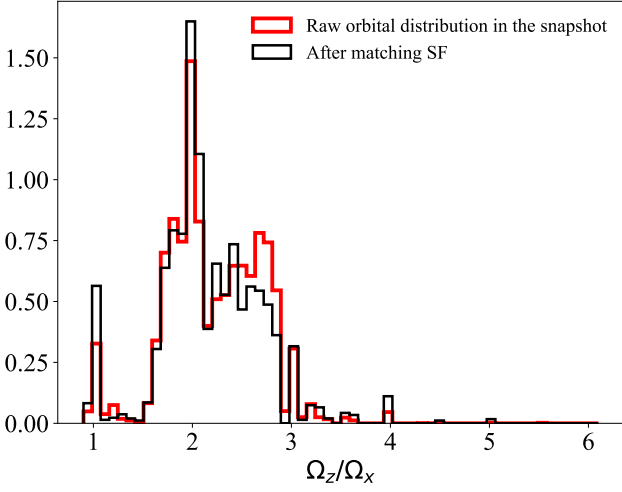


Figure A1. The effect of the selection function on orbital distribution is shown in this plot. The red and black lines are the orbital families before and after applying the selection function to Galaxy A, respectively.

APPENDIX B: SIDE-ON PROJECTION OF BAR ORBITS

The Galactic bar is composed of many orbital families classified by the Ω_Z/Ω_X value. Together, they assemble a boxy/peanut (BP) morphology with an X-shape structure embedded in an overall ellipsoidal density distribution. In Fig. B1, we present the side-on projection in each Ω_Z/Ω_X bin. The background is the density distribution by stacking the orbits of stars in each Ω_Z/Ω_X bin, which effectively represents the bar density contributed by this orbital family. Stars with smaller Ω_Z/Ω_X have more X-like shapes, while stars with larger Ω_Z/Ω_X are more elongated and boxy-like.

APPENDIX C: BAR LENGTH AND PATTERN SPEED MEASUREMENT WITH 15% DISTANCE UNCERTAINTY

As we discussed in Section 5.3, the heliocentric distance uncertainty could be underestimated in our sample, in which the fractional distance error could be as large as 15%. Therefore, we repeat the same analysis in Section 3.4 and 3.5 with 15% distance uncertainty. The blue dashed line in Fig. C1 is the radial $\langle |v_R/v_{\text{tot}}| \rangle$ value along the major axis of the bar after applying 15% distance uncertainty and the selection function. The difference between the radial profile before and after applying the observational caveats are still small.

Similar to Fig. 9, we show the bias on the pattern speed recovery caused by the observational uncertainty and selection function in Fig. C2 but with a 15% distance error. The bias is larger with the larger distance uncertainty, and the pattern speed is also consistently underestimated at high pattern speeds. However, the true and recovered pattern speeds still follow the 1:1 line, so we argue that the pattern speed estimation using the method in Dehnen et al. (2023) is still valid with the presence of 15% distance uncertainties and the incompleteness.

This paper has been typeset from a \LaTeX file prepared by the author.

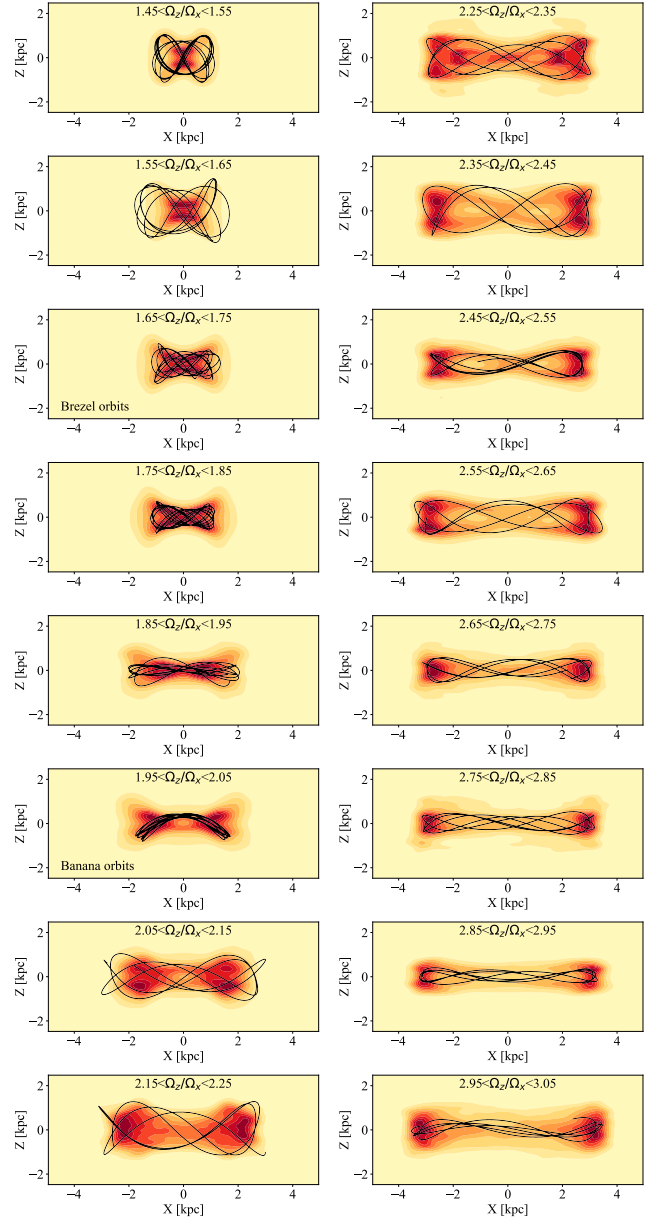


Figure B1. The side-on projection of orbital families in the Galactic bar. Stars are binned into Ω_Z/Ω_X segments as denoted in each panel. The background shows the density contributed by this orbital family by stacking the integrated orbits together. The overlaid line is a selected representative example of orbits in this family.

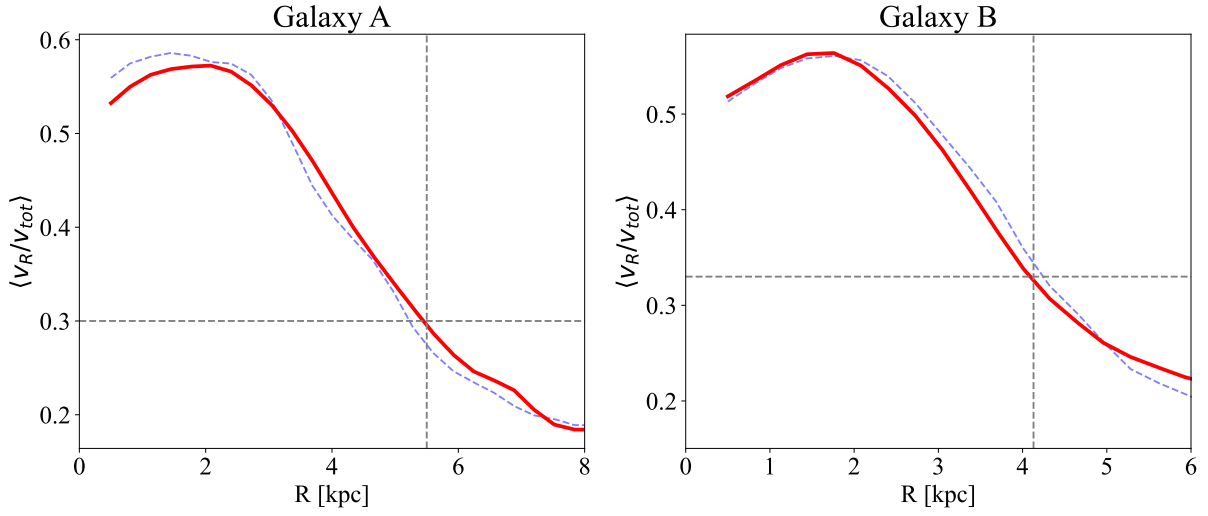


Figure C1. The radial $\langle |v_R/v_{tot}| \rangle$ along the bar major axis as a function of radius in Galaxy A (left) and B (right). The red line is the radial profile of the raw snapshot, and the blue dashed line is the radial profile after applying 15% distance uncertainty and the selection function.

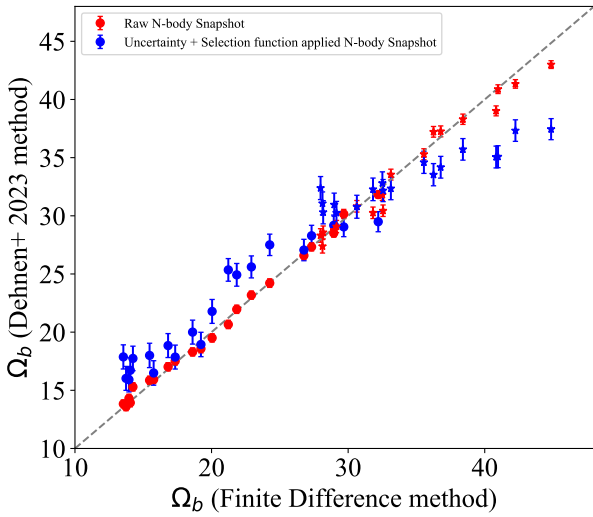


Figure C2. The recovered pattern speed compare to the true pattern speed for different N-body time snapshots. The red dots is the pattern speed estimate by applying the method in Dehnen et al. (2023) to the raw N-body snapshots, and the blue is that after applying 15% distance uncertainty and the selection function. The grey dashed line is the 1:1 line.